Inorganic Chemistry
Article
pubs.acs.org/IC

# Systematic Syntheses and Metalloligand Doping of Flexible Porous Coordination Polymers Composed of a Co(III)−Metalloligand

Atsushi Kobayashi,*[†,‡] Yui Suzuki,[†] Tadashi Ohba,[†] Tomohiro Ogawa,[†] Takeshi Matsumoto,[§] Shin-ichiro Noro,[∥] Ho-Chol Chang,[§] and Masako Kato*[†]

[†]Department of Chemistry, Faculty of Science, Hokkaido University, North-10 West-8, Kita-ku, Sapporo 060-0810, Japan

[‡]Japan Science and Technology Agency (JST), Precursory Research for Embryonic Science and Technology (PRESTO), Kawaguchi, Saitama 332-0012, Japan

[§]Department of Applied Chemistry, Faculty of Science and Engineering, Chuo University, 1-13-27 Kasuga, Bunkyo-ku, Tokyo 112-8551, Japan

[∥]Research Institute for Electronic Science, Hokkaido University, North-20, West-10, Kita-ku, Sapporo 001-0020, Japan

*Supporting Information*

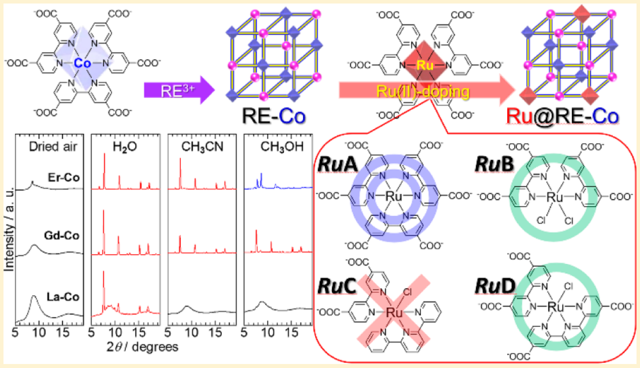

**ABSTRACT:** A series of flexible porous coordination polymers (PCPs) **RE−Co**, composed of a Co(III)−metalloligand $[Co(dcbpy)_3]^{3-}$ (**Co**; $H_2dcbpy$ = 4,4′-dicarboxy-2,2′-bipyridine) and lanthanide cations ($RE^{3+}$ = $La^{3+}$, $Ce^{3+}$, $Pr^{3+}$, $Nd^{3+}$, $Sm^{3+}$, $Eu^{3+}$, $Gd^{3+}$, $Tb^{3+}$, $Er^{3+}$), was systematically synthesized. X-ray crystallographic analysis revealed that the six carboxylates at the top of each coordination octahedron of Co(III)−metalloligand were commonly bound to $RE^{3+}$ cations to form a rock-salt-type porous coordination framework. When **RE−Co** contains a smaller and heavier $RE^{3+}$ cation than $Nd^{3+}$, the **RE−Co** crystallized in the cubic *Fm-3m* space group, whereas the other three **RE−Co** with larger $RE^{3+}$ crystallized in the lower symmetrical orthorhombic *Fddd* space group, owing to the asymmetric 10-coordinated bicapped square antiprism structure of the larger $RE^{3+}$ cation. Powder X-ray diffraction and vapor-adsorption isotherm measurements revealed that all synthesized **RE−Co** PCPs show reversible amorphous−crystalline transitions, triggered by water-vapor-adsorption/desorption. This transition behavior strongly depends on the kind of $RE^{3+}$; the transition of orthorhombic **RE−Co** was hardly observed under exposure to $CH_3OH$ vapor, but the **RE−Co** with smaller cations such as $Gd^{3+}$ showed the transition under exposure to $CH_3OH$ vapors. Further tuning of vapor-adsorption property was examined by doping of Ru(II)−metalloligands, $[Ru(dcbpy)_3]^{4-}$, $[Ru(dcbpy)_2Cl_2]^{4-}$, $[Ru(dcbpy)(tpy)Cl]^{-}$, and $[Ru(dcbpy)(dctpy)]^{3-}$ (abbreviated as ***Ru*A**, ***Ru*B**, ***Ru*C**, and ***Ru*D**, respectively; tpy = 2,2′:6′,2″-terpyridine, $H_2dctpy$ = 4,4″-dicarboxy-2,2′:6′,2″-terpyridine), into the Co(III)−metalloligand site of **Gd−Co** to form the Ru(II)-doped PCP ***Ru*X@Gd−Co** (X = A, B, C, or D). Three Ru(II)−metalloligands, ***Ru*A**, ***Ru*B**, and ***Ru*D** dopants, were found to be uniformly incorporated into the **Gd−Co** framework by replacing the original Co(III)−metalloligand, whereas the doping of ***Ru*C** failed probably because of the less number of coordination sites. In addition, we found that the ***Ru*A** doping into the **Gd−Co** PCP had a large effect on vapor-adsorption due to the electrostatic interaction originating from the negatively charged ***Ru*A** sites in the framework and the charge-compensating $Li^+$ cations in the porous channel.

## ■ INTRODUCTION

Porous materials have played important roles in physical, material, and biological chemistry because of their potential role in applications such as gas and vapor storage/separation, heterogeneous catalysis, and drug delivery.[1] Porous coordination polymers (PCPs) and metal−organic frameworks (MOFs), which are interesting porous materials composed of various metal ions connected via organic linkers, have recently been developed.[2−5] Taking advantage of their structural versatility, new physical properties have been reported, such as selective gas and vapor adsorption,[6−21] heterogeneous catalysis,[22−24] and external-stimuli-responsive magnetic and gas-adsorption properties,[25−28] which are hard to achieve using traditional inorganic and organic porous materials. One of the most advanced features of PCPs is the lattice flexibility derived from various coordination modes of the central metal ions and appropriate bonding strengths of the coordination bonds between metal ions and organic linkers.[14] This lattice flexibility enables the design of functional adsorbents, which can selectively adsorb certain gases and vapors. In addition to highly designable porosity, PCP systems have increasingly attracted

**Received:** September 2, 2014
**Published:** February 25, 2015

DOI: 10.1021/ic5021302
*Inorg. Chem.* 2015, 54, 2522−2535

attention not only because of their porosity but also because they act as a new field of integrating multiple functions.[29−41] Postsynthetic modification and postsynthetic metalation of the porous channels of PCPs are well-known techniques to functionalize these porous channels.[29−38] For example, Lin and co-workers reported on the incorporation of a highly active and enantioselective catalytic Ti(IV) site into the porous channels of a Cd(II)-based metal−organic framework by utilizing this method.[29] The other approach to introduce additional functionality into PCP is to utilize a metal complex ligand (known as metalloligands) as the linker for PCPs.[39−41] From the viewpoint of integration of multiple functions, using metalloligands as the linkers of a PCP framework is one of the most promising methods to develop multifunctional porous materials, because the molecule-based functions of metalloligands can be easily introduced into PCP frameworks.

Polypyridine metal complexes are well known to exhibit many interesting properties such as the photosensitization and reversible redox abilities of $[Ru(bpy)_3]^{2+}$,[42−44] spin transition of $[Co(tpy)_2]^{2+}$,[45,46] $H_2$-evolving catalysis of $[Co(bpy)_n]^{2+}$,[47−50] and $O_2$-evolving catalysis of $[Ru(bpy)(tpy)H_2O]^{2+}$.[51−53] This functional versatility has motivated many researchers to fabricate multifunctional PCPs based on the polypyridine metal complexes.[54−61] We also reported recently on the synthesis of two flexible PCP systems composed of tris-bipyridine-type Co(III)− or Ru(II)−metalloligands, $[M(dcbpy)_3]^{n-}$ (Scheme 1; M = $Co^{3+}$, $Ru^{2+}$; $n$ = 3 or 4; abbreviated as **Co**, ***Ru*A**; $H_2dcbpy$ = 4,4′-dicarboxy-2,2′-bipyridine), and found that the coordination networks of these PCP systems are flexible enough to exhibit reversible guest-adsorption-induced structural transformation.[62,63] In addition, the **RE−Co** PCPs composed of the **Co** and lanthanide cation $RE^{3+}$, $\{RE[Co(dcbpy)_3]\}$ ($RE^{3+}$ = $La^{3+}$, $Nd^{3+}$, $Gd^{3+}$), have large porosity (∼50%) and show interesting vapor-adsorption behaviors involving reversible amorphous−crystalline transition.[62] Notably, in spite of the very similar porous frameworks of **RE−Co**, the behavior strongly depends on the kind of $RE^{3+}$ cation; **La−Co** shows the amorphous−crystalline transition only under exposure to water vapor, but the transition of **Gd−Co** was observed not only in water vapor but also in $CH_3CN$ or $CH_3OH$ vapor.

**Scheme 1. Structural Representations of Polypyridine-Type Metalloligands Used in This Study**

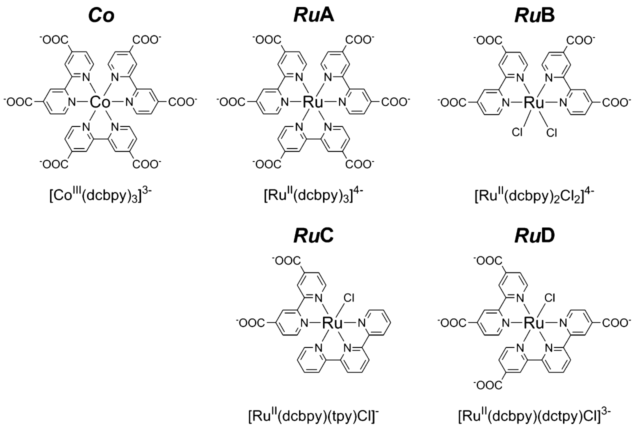

Therefore, in order to understand why the vapor-adsorption property strongly depends on the kind of $RE^{3+}$ cation, we recently focused on the systematic synthesis of **RE−Co** PCPs by using a series of lanthanide cations, which would enable us to control both the porosity and the vapor-adsorption behavior systematically.[64−66] Furthermore, taking advantage of the structural similarity of the metalloligands, we also investigated the doping of four different Ru(II) metalloligands, $[Ru(dcbpy)_3]^{4-}$, $[Ru(dcbpy)_2Cl_2]^{4-}$, $[Ru(dcbpy)(tpy)Cl]^{-}$, and $[Ru(dcbpy)(dctpy)]^{3-}$ (Scheme 1; abbreviated as ***Ru*A**, ***Ru*B**, ***Ru*C**, and ***Ru*D**, respectively; tpy = 2,2′:6′,2″-terpyridine, $H_2dctpy$ = 4,4″-dicarboxy-2,2′:6′,2″-terpyridine) into the **Gd−Co** PCPs, because the doping and/or mixing of functional ligands into a PCP framework has recently been recognized as a new powerful technique to widely modulate the guest-adsorption property.[67−71] In addition, this doping study based on the four Ru(II) metalloligands with different numbers of coordination sites may enable us to clarify the structural parameters required for the metalloligand dopant. This information could be basically important and beneficial to construct multifunctional porous materials, e.g., heterogeneous catalyst, solid electrolyte, and so on. Herein, we report on the syntheses, crystal structures, structural transition behaviors, and vapor-adsorption properties of six newly obtained **RE−Co** PCPs ($RE^{3+}$ = $Ce^{3+}$, $Pr^{3+}$, $Sm^{3+}$, $Eu^{3+}$, $Tb^{3+}$, $Er^{3+}$) and the Ru(II)−metalloligand-doped PCP, ***Ru*X@Gd−Co**, and demonstrate that the coordination geometry of the $RE^{3+}$ ion in the **RE−Co** porous framework plays an important role in the vapor-adsorption-triggered structural transformation. We also demonstrate that three Ru(II)−metalloligands, ***Ru*A**, ***Ru*B**, and ***Ru*D**, bearing six or four coordinating $COO^-$ groups have been successfully incorporated into the **Gd−Co** framework and the ***Ru*A** doping significantly affected the vapor-adsorption property, probably due to the more negatively charged ***Ru*A** coupled with the $Li^+$ incorporation into the porous channels of **Gd−Co**.

## ■ EXPERIMENTAL SECTION

**General Procedures.** All commercially available starting materials, $LaCl_3·7H_2O$, $CeCl_3·7H_2O$, $PrCl_3·7H_2O$, $NdCl_3·6H_2O$, $SmCl_3·6H_2O$, $EuCl_3·6H_2O$, $GdCl_3·6H_2O$, $TbCl_3·6H_2O$, and $ErCl_3·6H_2O$, were used as received, and solvents were used without any purification. Unless otherwise stated, all manipulations were conducted in air. The starting Co(III)−metalloligand, $[Co(Hdcbpy)_3]·6H_2O$, Ru(II)−metalloligands, $[Ru(H_2dcbpy)(Hdcbpy)_2]$, $[Ru(H_2dcbpy)_2Cl_2]$, $[Ru(H_2dcbpy)(tpy)Cl]Cl$, and $[Ru(H_2dcbpy)(H_2dctpy)Cl]Cl$ ($H_4$***Ru*A**, $H_4$***Ru*B**, $H_2$***Ru*C** or $H_4$***Ru*D**), were prepared according to previously published methods.[72−74] Elemental analysis was conducted at the Analysis Center, Hokkaido University.

**Synthesis of $\{RE[Co(dcbpy)_3]·nH_2O\}$ (RE−Co; M = $La^{3+}$, $Ce^{3+}$, $Pr^{3+}$, $Nd^{3+}$, $Nd^{3+}$, $Sm^{3+}$, $Eu^{3+}$, $Gd^{3+}$, $Tb^{3+}$, and $Er^{3+}$).** All **RE−Co** PCPs were prepared by the method previously reported.[62] Typically, a solution of $RECl_3·nH_2O$ ($3.96 \times 10^{-2}$ mmol) in EtOH (1 mL) was carefully layered on top of a solution of $[Co(Hdcbpy)_3]·6H_2O$ (20.0 mg, $2.23 \times 10^{-2}$ mmol) in ammonia−water (2 mL, pH = 10.2). Pale-yellow platelet or block crystals began to form after several days. One of these crystals was used for single-crystal X-ray crystallography. After 1 week, these crystals were collected by filtration, washed with water, and dried under vacuum for 1 h. **La−Co**: yield 13.6 mg, 71.4% based on $[Co(Hdcbpy)_3]·6H_2O$. Anal. Calcd for $C_{36}H_{18}Co_1La_1N_6O_{12}·14H_2O$: C, 36.75; H, 3.94; N, 7.14. Found: C, 36.84; H, 3.47; N, 7.19. **Ce−Co**: yield 8.16 mg, 41.2% based on $[Co(Hdcbpy)_3]·6H_2O$. Anal. Calcd for $C_{36}H_{18}Co_1Ce_1N_6O_{12}·7H_2O$: C, 41.11; H, 3.07; N, 7.99. Found: C, 41.32; H, 3.11; N, 8.17. **Pr−Co**: yield 17.4 mg, 80.8% based on $[Co(Hdcbpy)_3]·6H_2O$. Anal. Calcd for $C_{36}H_{18}Co_1Pr_1N_6O_{12}·6H_2O$: C, 41.80; H, 2.92; N 8.12. Found: C, 41.52; H, 3.24; N, 7.93. **Nd−Co**: yield 17.2 mg, 65.3% based on $[Co(Hdcbpy)_3]·6H_2O$. Anal. Calcd for $C_{36}H_{18}Co_1Nd_1N_6O_{12}·14H_2O$: C, 36.58; H, 3.92; N, 7.11. Found: C, 36.36; H, 3.74; N, 7.16. **Sm−Co**: yield 10.8 mg, 54.0% based on

DOI: 10.1021/ic5021302
*Inorg. Chem.* 2015, 54, 2522−2535

[Co(Hdcbpy)$_3$]·6H$_2$O. Anal. Calcd for $C_{36}H_{18}Co_1Sm_1N_6O_{12}\cdot 11H_2O$: C, 38.13; H, 3.56; N, 7.41. Found: C, 37.84; H, 3.50; N, 7.43. **Eu−Co**: yield 9.0 mg, 48.5% based on [Co(Hdcbpy)$_3$]·6H$_2$O. Anal. Calcd for $C_{36}H_{18}Co_1Eu_1N_6O_{12}\cdot 11H_2O$: C, 38.08; H, 3.55; N, 7.40. Found: C, 38.27; H, 3.84; N, 7.11. **Gd−Co**: yield 13.2 mg, 49.5% based on [Co(Hdcbpy)$_3$]·6H$_2$O. Anal. Calcd for $C_{36}H_{18}Co_1Gd_1N_6O_{12}\cdot 14H_2O$: C, 36.18; H, 3.88; N, 7.03. Found: C, 36.03; H, 3.67; N, 7.08. **Tb−Co**: yield 8.4 mg, 42.6% based on [Co(Hdcbpy)$_3$]·6H$_2$O. Anal. Calcd for $C_{36}H_{18}Co_1Tb_1N_6O_{12}\cdot 12H_2O$: C, 37.26; H, 3.65; N, 7.24. Found: C, 37.21; H, 3.71; N, 7.23. **Er−Co**: yield 8.99 mg, 46.5% based on [Co(Hdcbpy)$_3$]·6H$_2$O. Anal. Calcd for $C_{36}H_{18}Co_1Er_1N_6O_{12}\cdot 10H_2O$: C, 38.17; H, 3.38; N, 7.42. Found: C, 38.09; H, 3.40; N, 7.00.

**Syntheses of Ru(II)−Metalloligand-Doped Gd−Co.** All Ru(II)−metalloligand-doped **Gd−Co**, ***Ru*X@Gd−Co** (**X** = **A**, **B**, **C**, or **D**), were prepared by the following procedure. Typically, two metalloligands, [Co(Hdcbpy)$_3$] (16.0 mg, 0.020 mmol), Ru(II)−metalloligand (***Ru*A**, ***Ru*B**, ***Ru*C**, or ***Ru*D**, 4.7 $\mu$mol), and LiCl (10.0 mg, 0.234 mmol) were dissolved in ammonia−water (2 mL, pH = 10.2). On the top of this mixed aqueous solution, ethyl acetate (1 mL) and an EtOH (1 mL) solution of GdCl$_3$·6H$_2$O (15.0 mg, 0.040 mmol) were carefully layered. Block crystals began to form after several days. After allowing the solution to stand for 2 weeks, these crystals were collected by filtration, washed with water, and dried under vacuum for 1 h. The obtained four different Ru(II)-doped **Gd−Co** were analyzed by scanning electron microscopy (SEM), energy-dispersive X-ray spectroscopy (EDS), and inductively coupled plasma/atomic emission spectroscopy (ICP-AES) to estimate the Ru(II)−dopant concentration in **Gd−Co** framework. In addition, powder X-ray diffraction and UV−vis absorption spectroscopy were conducted to evaluate not only the crystal structure in the bulk sample but also the molecular structure around the Ru(II)−metalloligand. ***Ru*A@Gd−Co**: Reddish-orange block crystals. Yield: 7.69 mg 32.3% based on the total molar amount of two metalloligands. Anal. Calcd for GdLi$_{0.2}$[Co(dcbpy)$_3$]$_{0.8}$ [Ru(dcbpy)$_3$]$_{0.2}$·11H$_2$O: C, 37.58; H, 3.50; N, 7.30. Found: C, 37.64; H, 3.21; N, 7.41. ***Ru*B@Gd−Co**: Reddish-orange block crystals. Yield: 4.95 mg 26.8% based on the total molar amount of two metalloligands. ***Ru*C@Gd−Co**: Brownish-yellow block crystals. Yield: 6.05 mg 31.4% based on the total molar amount of two metalloligands. ***Ru*D@Gd−Co**: Reddish-orange block crystals. Yield: 8.39 mg 43.6% based on the total molar amount of two metalloligands.

**Single-Crystal X-ray Diffraction Measurements.** All single-crystal X-ray diffraction measurements, except for the orthorhombic crystal of **Pr−Co**, were conducted using a Rigaku Mercury CCD diffractometer with graphite-monochromated Mo K$\alpha$ radiation ($\lambda$ = 0.71069 Å) and a rotating anode generator. The measurements for orthorhombic **Pr−Co** were conducted by the same type of diffractometer at the NW2A beamline of the Advanced Ring, Photon Factory, KEK, Japan. The wavelength of the synchrotron X-ray was 0.6890(1) Å. Each single crystal was mounted on a MicroMount using paraffin oil. The crystal was then cooled using a N$_2$-flow-type temperature controller. Diffraction data were collected and processed using the Crystal Clear software package.[75] Structures were solved by direct methods using SIR-2004.[76] Structural refinements were conducted by the full-matrix least-squares method using SHELXL-97.[77] Non-hydrogen atoms were refined anisotropically; hydrogen atoms were refined using the riding model. All calculations were conducted using the Crystal Structure crystallographic software package.[78] Crystallographic data obtained for each complex are summarized in Table 1. Full crystallographic details have been deposited with the Cambridge Crystallographic Data Centre as supplementary publication No. CCDC-1021754 for **Ce−Co**, CCDC-1021755 for orthorhombic **Pr−Co**, CCDC-1021756 for cubic **Pr−Co**, CCDC-1021757 for **Sm−Co**, CCDC-1021758 for **Eu−Co**, CCDC-1021759 for **Tb−Co**, and CCDC-1021760 for **Er−Co**.

**Powder X-ray Diffraction.** Powder X-ray diffraction was conducted using a Rigaku SPD diffractometer at the BL-8B beamline at the Photon Factory, KEK, Japan, or a Bruker D8 Advance diffractometer equipped with a graphite monochrometer using Cu K$\alpha$ radiation and a one-dimensional LinxEye detector. The wavelength of

Table 1. Crystal Parameters and Refinement Data of RE−Co PCPs

| | La−Co[a] | Ce−Co | Pr−Co (ortho) | Pr−Co (cubic) | Nd−Co[a] | Sm−Co | Eu−Co | Gd−Co[a] | Tb−Co | Er−Co |
|---|---|---|---|---|---|---|---|---|---|---|
| $T$/K | 150(1) | 150(1) | 150(1) | 150(1) | 153(1) | 150(1) | 158(1) | 150(1) | 153(1) | 150 |
| formula | $C_{36}H_{18}N_6O_{12}CoLa$ | $C_{36}H_{18}CeCoN_6O_{12}\cdot 26H_2O$ | $C_{36}H_{18}CoN_6O_{12}Pr\cdot 22H_2O$ | $C_{36}H_{18}CoN_6O_{12}Pr$ | $C_{36}H_{18}N_6O_{12}CoNd$ | $C_{36}H_{18}CoN_6O_{12}Sm$ | $C_{36}H_{18}CoEuN_6O_{12}$ | $C_{36}H_{18}N_6O_{12}CoGd$ | $C_{36}H_{18}CoN_6O_{12}Tb$ | $C_{36}H_{18}CoErN_6O_{12}$ |
| fw | 924.41 | 1394.02 | 1322.75 | 926.41 | 929.74 | 935.90 | 937.46 | 942.75 | 944.43 | 952.76 |
| cryst syst | orthorhombic | orthorhombic | orthorhombic | cubic | cubic | cubic | cubic | cubic | cubic | cubic |
| space group | *Fddd* (#70) | *Fddd* (#70) | *Fddd* (#70) | *Fm*-3*m* (#225) | *Fm*-3*m* (#225) | *Fm*-3*m* (#225) | *Fm*-3*m* (#225) | *Fm*-3*m* (#225) | *Fm*-3*m* (#225) | *Fm*-3*m* (#225) |
| $a$/Å | 23.522(3) | 23.420(7) | 23.316(5) | 17.982(9) | 18.1481(10) | 18.027(5) | 18.014(5) | 17.9966(7) | 17.9076(10) | 17.8277(10) |
| $b$/Å | 28.077(4) | 28.043(8) | 28.011(6) | | | | | | | |
| $c$/Å | 36.438(5) | 36.241(10) | 36.079(7) | | | | | | | |
| $V$/Å$^3$ | 24064(5) | 23801(11) | 23563(8) | 5815(5) | 5977.1(6) | 5858(3) | 5845(3) | 5828.7(4) | 5742.6(6) | 5666.1(6) |
| $Z$ | 16 | 16 | 16 | 4 | 4 | 4 | 4 | 4 | 4 | 4 |
| $D_{calcd}$/g·cm$^{-3}$ | 1.021 | 1.556 | 1.491 | 1.058 | 1.033 | 1.061 | 1.065 | 1.074 | 1.092 | 1.117 |
| no. of reflns collected | 28 321 | 46 073 | 127 739 | 11 437 | 11 891 | 11 644 | 11 776 | 11 901 | 11 604 | 11 374 |
| no. of unique reflns | 6880 | 6804 | 13 810 | 390 | 399 | 395 | 392 | 390 | 388 | 383 |
| GOF | 1.062 | 1.316 | 1.135 | 1.424 | 1.285 | 1.311 | 1.271 | 1.234 | 1.208 | 1.186 |
| $R_{int}$ | 0.076 | 0.0554 | 0.0645 | 0.0447 | 0.028 | 0.0294 | 0.0283 | 0.028 | 0.0314 | 0.0358 |
| $R$ ($I > 2.00\sigma(I)$) | 0.075 | 0.0832 | 0.0709 | 0.1055 | 0.082 | 0.0763 | 0.0753 | 0.075 | 0.0749 | 0.0762 |
| $R_W$[b] | 0.292 | 0.1569 | 0.2579 | 0.2788 | 0.241 | 0.2452 | 0.2424 | 0.239 | 0.2231 | 0.2188 |

[a] Reference 62. [b] $RW = [\Sigma(w(F_0^2 - F_c^2)^2)/\Sigma w(F_0^2)^2]^{1/2}$.

the synchrotron X-ray was 1.200(1) Å. All samples were placed in a glass capillary with a diameter of 0.5 mm.

**Thermogravimetric Analysis.** Thermogravimetry and differential thermal analysis were conducted using a Rigaku ThermoEvo TG8120 analyzer.

**Adsorption Isotherms.** The adsorption isotherms for $H_2O$, $CH_3CN$, and $CH_3OH$ vapors at 298 K were performed using an automatic volumetric adsorption apparatus (BELSORP-MAX and BELSORP-aqua; BEL Japan, Inc.).

**UV−Vis Spectroscopy.** The UV−vis diffuse reflectance spectrum of each PCP was recorded on a Shimadzu UV-2400PC spectrophotometer equipped with an integrating sphere apparatus. The reflectance spectra obtained were converted to absorption spectra using the Kubelka−Munk function $F(R_\infty)$.

**IR Spectroscopy.** The IR spectrum of each complex was recorded on a Nicolet 6700 FT-IR spectrometer equipped with a Smart-Orbit (Diamond) ATR accessory.

**Scanning Electron Microscopy (SEM) and Energy-Dispersive X-ray Spectroscopy (EDS) Analyses.** SEM/EDS images and data were collected using a JEOL JSM-6360-LA analytical scanning electron microscope. Samples were mounted on a carbon-coated tape. The energy of the electron beam was 30 kV, and all of the data were calibrated with standards.

**Inductively Coupled Plasma/Atomic Emission Spectroscopy (ICP-AES).** Each sample (1 mg) was dissolved in 60% $HNO_3$ (aq) and heated at 398 K for several hours to remove all organic components. The resultant solid was dissolved in 0.1 M $HNO_3$ aqueous solution (20 mL), filtered by using 0.1 $\mu m\phi$ membrane filter (Melck, Omnipore JV), and then analyzed using a Shimadzu ICPE-9000 spectrometer.

## ■ RESULTS AND DISCUSSION

**Crystal Structures of RE−Co PCPs.** We previously reported on the crystal structures of **La−Co**, **Nd−Co**, and **Gd−Co** and found that these PCPs commonly had rock-salt-type porous frameworks built from the Co(III)−metalloligand and $RE^{3+}$ ion.[62] Interestingly, the two enantiomers, Δ- and Λ-$[Co(dcbpy)_3]^{3-}$, were completely ordered in only **La−Co** to form a lower symmetric orthorhombic *Fddd* structure, but they were disordered in the structures of **Nd−Co** and **Gd−Co** to form a higher symmetric cubic *Fm-3m* structure. In order to systematically control the porosity of the **RE−Co** system and to investigate the origin of the enantiomer ordering in **La−Co**, we prepared **RE−Co** PCPs composed of a series of lanthanide ions. We found that the **RE−Co** with a larger and lighter $RE^{3+}$ ion than $Nd^{3+}$ crystallized in the same orthorhombic *Fddd* space group as **La−Co** and that the other **RE−Co** with smaller and heavier $RE^{3+}$ ions crystallized in the cubic *Fm-3m* space group, as did **Gd−Co**. This result clearly indicates that the ionic radius of the $RE^{3+}$ ion plays an important role in the structure of **RE−Co** PCPs.

Figure 1 shows the crystal structure of **Ce−Co**. Selected bond lengths are summarized in Table 2. Structural parameters regarding the porosity of **RE−Co** PCPs are given in Table 3. **Ce−Co** and **Pr−Co** PCPs with larger $RE^{3+}$ ions than $Nd^{3+}$ crystallized in the isomorphic orthorhombic *Fddd* space group. As shown in Figure 1, the Co(III)−metalloligand $[Co(dcbpy)_3]^{3-}$ is coordinated to six $RE^{3+}$ ions to form a three-dimensional porous framework, like that observed for all **RE−Co** PCPs. The Co−N bond distances (1.925(6)−1.944(6) Å) indicate that the Co ion remains in the trivalent oxidation state. In the case of the orthorhombic structures of **Ce−Co** and **Pr−Co**, the two enantiomers, Δ- and Λ-$[Co(dcbpy)_3]^{3-}$, were completely ordered at two different Co(III) sites as well as **La−Co**. Two of the six carboxylates were directed to the *c* axis and coordinated in a monodentate fashion (Figure 1c), while the other four were coordinated in the *ab* plane in a bidentate fashion. Thus, the $RE^{3+}$ ion adopts a 10-coordinated bicapped square antiprism structure. All four bidentate carboxylates in the *ab* plane were tilted toward the same direction. As a result, only one kind (Δ or Λ) of $[Co(dcbpy)_3]^{3-}$ enantiomer can be located in the same *ab* plane. Consequently, three kinds of porous channels with different window sizes were formed along the *a* + *b* axis, as shown in Figure 1a. Although all kinds of porous channels are surrounded by four dcbpy ligands, the differences between the channels are derived from the direction of the bipyridine plane toward the channel. One channel (denoted by A) was surrounded by dcbpy ligands, whose bipyridyl planes were parallel to the channel direction. Another channel (B) was surrounded by two dcbpy ligands that were parallel and two dcbpy ligands that were perpendicular to the channel direction. The final channel (C) was surrounded by one parallel and three perpendicular dcbpy ligands to form the porous channel with the smallest window size. As expected from the lanthanide contraction, both the window size of porous channel and the void fraction decreased in the order **La−Co** > **Ce−Co** > **Pr−Co** with contraction of the $RE^{3+}$ ionic radius (see Table 3).

Figure 2 shows the crystal structure of **Er−Co**. In contrast to **RE−Co** with larger $RE^{3+}$, two enantiomers of $[Co(dcbpy)_3]^{3-}$ were completely disordered in all cubic structures of **RE−Co** with smaller $RE^{3+}$ ions than $Pr^{3+}$. We found that cubic crystals of **Pr−Co** were also obtained as a very minor product. Judging from the short Co−N bond distances (1.87(2)−1.899(2) Å), the Co ion remains in the trivalent oxidation state. The RE−O bond distance simply decreased according to the lanthanide contraction effect. In this cubic structure, all of the carboxylates seemed to coordinate to the $RE^{3+}$ ion in a bidentate fashion, resulting in the formation of only one kind of porous channel with diameters varying from 4.12 Å for **Sm−Co** to 3.82 Å for **Er−Co**. Because of the presence of six bidentate carboxylates, the coordination number of the $RE^{3+}$ ions seems to be 12. However, it is well known that small $RE^{3+}$ ions such as $Er^{3+}$ generally cannot adopt a 12-coordinated structure. To clarify the coordination environment of the $RE^{3+}$ ion in the cubic structure, IR spectroscopy was performed because the vibration of the C═O bond in the carboxylate strongly depends on the coordination mode. The observed IR spectra of these PCPs were almost identical to that of the orthorhombic **Ce−Co** and clearly show two couples of asymmetric and symmetric vibration modes of C═O bonds (see Figure S1, Supporting Information), suggesting that the carboxylates of the $[Co(dcbpy)_3]^{3-}$ ligand are coordinated by both the monodentate and the bidentate modes. Considering the fact that even the $La^{3+}$ ion with the largest ionic radius in the lanthanide series has a 10-coordinated structure, the coordination number of the $RE^{3+}$ ion that is smaller than $Pr^{3+}$ should be less than 10. These results also suggest that the reason why only **RE−Co**, with larger $RE^{3+}$ ions than $Nd^{3+}$, crystallized in the orthorhombic structure with the ordering of two $[Co(dcbpy)_3]^{3-}$ enantiomers. These larger $RE^{3+}$ ions have a sufficiently large coordination space around the $RE^{3+}$ ion to form the 10-coordinated bicapped square antiprism structure, which is one of the most important structural factors for the ordering of $[Co(dcbpy)_3]^{3-}$ enantiomers. Only the RE−O5 distance elongated in the order **La−Co** < **Ce−Co** < **Pr−Co**, while the other RE−O distances shortened according to the ionic radius of the $RE^{3+}$ ion (see Table 2). Thus, the $RE^{3+}$ ions that are smaller than $Pr^{3+}$ cannot adopt the 10-coordinated

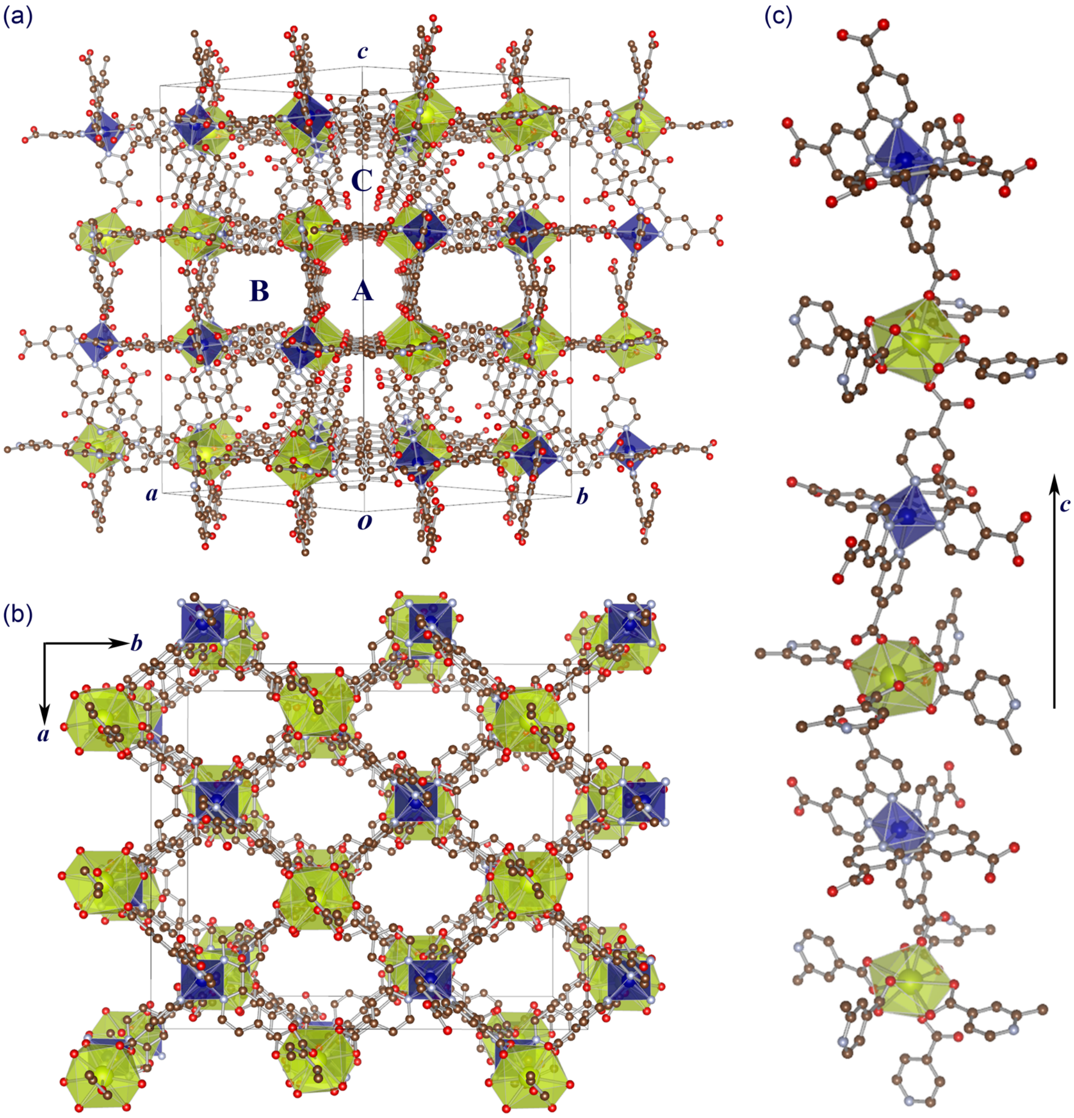

**Figure 1.** Packing diagrams of **Ce−Co** PCP viewed along the (a) *a* + *b* and (b) *c* axes. (c) Alternate stacking structure along the *c* axis, built from $Ce^{3+}$ and $[Co(dcbpy)_3]^{3-}$. Three kinds of pores are denoted by A, B, and C in a. Coordination spheres of Co(III) and Ce(III) ions are shown as blue and yellow-green polyhedrons, respectively. Brown, light blue, and red balls represent C, N, and O atoms, respectively. Noncoordinated water molecules and H atoms are omitted for clarity.

bicapped square antiprism structure, resulting in the disordering of the two enantiomers, Δ- and Λ-$[Co(dcbpy)_3]^{3-}$.

Figure 3 shows the relationship between the ionic radius of $RE^{3+}$ ion and the unit cell volume, void volume, and void fraction of **RE−Co** PCPs. The void volumes were estimated by using the *PLATON SQUEEZE* program[79] in which the noncoordinated water molecules in the porous channels are excluded. As expected from lanthanide contraction, both unit cell and void volumes of **RE−Co** are almost proportional to the ionic radius of $RE^{3+}$ except for the cubic **Pr−Co**, resulting in the large void fraction ranging from 47.4% (**Er−Co**) to 55.0% (**La−Co**). Thus, these PCPs are expected to adsorb a large amount of guest molecules in the large pores. In fact, X-ray crystallographic analyses for the orthorhombic **Ce−Co** and **Pr−Co** PCPs revealed the presence of large numbers of water molecules in the porous channels.

**Guest-Induced Amorphous−Crystalline Transition of RE−Co PCPs.** As mentioned in the Introduction, we previously reported that the porous frameworks of **La−Co**, **Nd−Co**, and **Gd−Co** PCPs were flexible enough to exhibit a reversible amorphous−crystalline transition driven by guest release/adsorption.[62] Interestingly, the porous frameworks of all these three PCPs were regenerated by water vapor adsorption, but only the framework of the **Gd−Co** PCP was also regenerated by the adsorption of $CH_3OH$ and $CH_3CN$ vapor. This difference implies that the $RE^{3+}$ ion plays a critical role in the guest-induced amorphous−crystalline transition behavior. Thus, in order to investigate this role in more detail, we measured the changes in the powder X-ray diffraction (PXRD) patterns of the newly synthesized six **RE−Co** PCPs ($RE^{3+}$ = $Ce^{3+}$, $Pr^{3+}$, $Sm^{3+}$, $Eu^{3+}$, $Tb^{3+}$, $Er^{3+}$) as well as those for **La−Co**, **Nd−Co**, and **Gd−Co** PCPs.[51]

Figure 4 shows the PXRD patterns of each of these nine **RE−Co** PCPs under exposure to dried air, saturated $H_2O$, $CH_3CN$, and $CH_3OH$ vapor, in comparison to the simulated patterns of the orthorhombic **La−Co** and cubic **Gd−Co**. Each sample was dried overnight under vacuum before conducting the measurements. TG analysis showed that the chemical

Table 2. Bond Lengths (Å) Around Co$^{3+}$ and RE$^{3+}$ Ions of **RE–Co** PCPs

| | La–Co[a] | Ce–Co | Pr–Co (ortho) | Pr–Co (cubic) | Nd–Co[a] | Sm–Co | Eu–Co | Gd–Co[a] | Tb–Co | Er–Co |
|---|---|---|---|---|---|---|---|---|---|---|
| Co1–N1 | 1.944(6) | 1.935(5) | 1.937(3) | 1.87(2) | 1.895(2) | 1.896(2) | 1.899(2) | 1.888(2) | 1.889(2) | 1.88(3) |
| Co1–N2 | 1.931(6) | 1.932(5) | 1.939(3) | | | | | | | |
| Co1–N3 | 1.925(6) | 1.926(5) | 1.933(3) | | | | | | | |
| sum of ionic radii of RE$^{3+}$ and O$^{2-}$ [b] | 2.560 | 2.543 | 2.526 | 2.526 | 2.509 | 2.479 | 2.466 | 2.453 | 2.440 | 2.404 |
| RE–O1 | 2.593(5) | 2.570(4) | 2.555(3) | 2.63(3) | 2.57(2) | 2.52(3) | 2.50(3) | 2.46(2) | 2.41(3) | 2.36(3) |
| RE–O2 | 2.651(6) | 2.651(5) | 2.614(4) | | | | | | | |
| RE–O4 | 2.426(5) | 2.401(4) | 2.383(4) | | | | | | | |
| RE–O5 | 2.714(6) | 2.732(5) | 2.740(5) | | | | | | | |
| RE–O6 | 2.616(7) | 2.576(6) | 2.551(5) | | | | | | | |

[a] Reference 62. [b] Reference 81 in the 8-coordinated structure.

Table 3. Structural Parameters Regarding the Porosity of **RE–Co** PCPs

| complex | void volume (Å$^3$) | void fraction (%) | pore diameter (Å) |
|---|---|---|---|
| **La–Co**[a] | 13 236 | 55.0 | A 6.78 × 5.86<br>B 7.13 × 4.13<br>C 5.06 × 4.30 |
| **Ce–Co** | 13 008 | 54.4 | A 6.80 × 5.75<br>B 7.18 × 4.03<br>C 4.98 × 4.27 |
| **Pr–Co** (ortho) | 12 704 | 53.9 | A 6.76 × 5.72<br>B 7.18 × 3.97<br>C 4.94 × 4.24 |
| **Pr–Co** (cubic) | 2893 | 49.8 | 4.16 |
| **Nd–Co**[a] | 3041 | 50.9 | 4.18 |
| **Sm–Co** | 2901 | 49.5 | 4.12 |
| **Eu–Co** | 2909 | 49.8 | 4.10 |
| **Gd–Co**[a] | 2884 | 49.5 | 4.03 |
| **Tb–Co** | 2776 | 48.3 | 3.97 |
| **Er–Co** | 2685 | 47.4 | 3.82 |

[a] Reference 62.

composition of the **RE–Co** framework (except for hydrated water molecules) does not change by the drying process (see Figure S2, Supporting Information). In addition, almost identical PXRD patterns of **RE–Co** PCPs before drying to the simulations indicate that the samples are pure enough to discuss the structural transformation induced by vapor adsorption (see Figure S3, Supporting Information). Similar to the previous three **RE–Co** PCPs, all **RE–Co** PCPs show broad featureless amorphous-like patterns in dried air, suggesting that the porous frameworks of the other six **RE–Co** PCPs are also not sufficiently rigid to retain the porous structure without water of crystallization. This can be attributed to the large void fraction (over 45%) and/or flexible coordination mode of the RE$^{3+}$ ion. On the other hand, the observed PXRD patterns of all **RE–Co** PCPs in saturated water vapor agreed well with the simulation patterns of orthorhombic or cubic **RE–Co** PCPs, as shown in Figure 4b, indicating that the porous frameworks of the **RE–Co** PCPs were regenerated by the adsorption of water vapor. Interesting differences were observed for the saturated $CH_3CN$ and $CH_3OH$ vapor, as shown in Figure 4c and 4d. Although the PXRD patterns of **La–Co** did not change under these polar organic vapors, the other orthorhombic **RE–Co** PCPs, **Ce–Co**, and **Pr–Co** showed sharp crystalline patterns that agreed with the simulation of the orthorhombic phase in the saturated $CH_3CN$ vapor, but the original amorphous-like patterns were hardly changed in the $CH_3OH$ vapor. This difference clearly indicates that the guest-induced amorphous–crystalline transition behavior depended strongly on the kind of RE$^{3+}$ ion that was used. A similar dependence on the RE$^{3+}$ ion was also observed for the cubic **RE–Co** PCPs. Under exposure of the dried samples to saturated $CH_3CN$ vapor, the PXRD patterns of the other cubic **RE–Co** PCPs were changed from the broad amorphous-like to the sharp crystalline patterns, which are in good agreement with their simulations. In contrast, only **Gd–Co** clearly showed the almost identical pattern to that obtained by simulation under exposure to $CH_3OH$ vapor. In addition, the **Er–Co** showed a different PXRD pattern from that of dried or $H_2O$-vapor-exposed ones, suggesting that the structure of **Er–Co** under exposure to $CH_3OH$ is different from that determined by single-crystal X-ray diffraction for the hydrated **Er–Co** crystal. Under exposure to other organic vapors (ethanol, acetone, $CHCl_3$, toluene, etc.), no **RE–Co** PCPs exhibited the amorphous–crystalline transition behavior (see Figures S4 and S5, Supporting Information). Thus, the guest-induced amorphous–crystalline transition behavior of **RE–Co** PCPs clearly depends on the kind of RE$^{3+}$ ion. The reason why the transition could be induced by only three small polar vapors is probably that the porous channels of **RE–Co** PCPs are formed by a large number of hydrophilic carboxyl groups that bonded to the RE$^{3+}$ ions. The pore size is another important factor, i.e., large hydrophilic molecules as *i*-PrOH and DMSO could not be adsorbed in the porous channels. The transition cannot be induced by $CH_3OH$ vapor for the orthorhombic **RE–Co** PCPs with La$^{3+}$, Ce$^{3+}$, and Pr$^{3+}$ but can be induced for the cubic **RE–Co** PCPs with smaller RE$^{3+}$. This remarkable difference could be derived from the differences in the character of the porous channels. As discussed in the Crystal Structures of **RE–Co** PCPs section, the pore diameter of all **RE–Co** PCPs is sufficiently large (>3.8 Å) for the $CH_3OH$ molecule, but the structural disordering of the cubic **RE–Co** PCPs comprises two enantiomers of Co(III)–metalloligand. As a result, the ratio of the monodentate carboxylate to the bidentate one should be larger in the cubic **RE–Co** PCPs than that in the orthorhombic one (monodentate:bidentate = 2:4). This monodentate carboxylate would interact with the adsorbed $CH_3OH$ more effectively than with the bidentate one, resulting in the amorphous–crystalline transition of cubic **RE–Co** PCPs in the $CH_3OH$ vapor. The clear transition behavior of **Gd–Co** may be related to the size of the RE$^{3+}$ site in the cubic structure. Single-crystal X-ray analysis for the cubic **RE–Co** only revealed the averaged RE–O distance because of the disordering of the Co(III)

DOI: 10.1021/ic5021302
Inorg. Chem. 2015, 54, 2522–2535

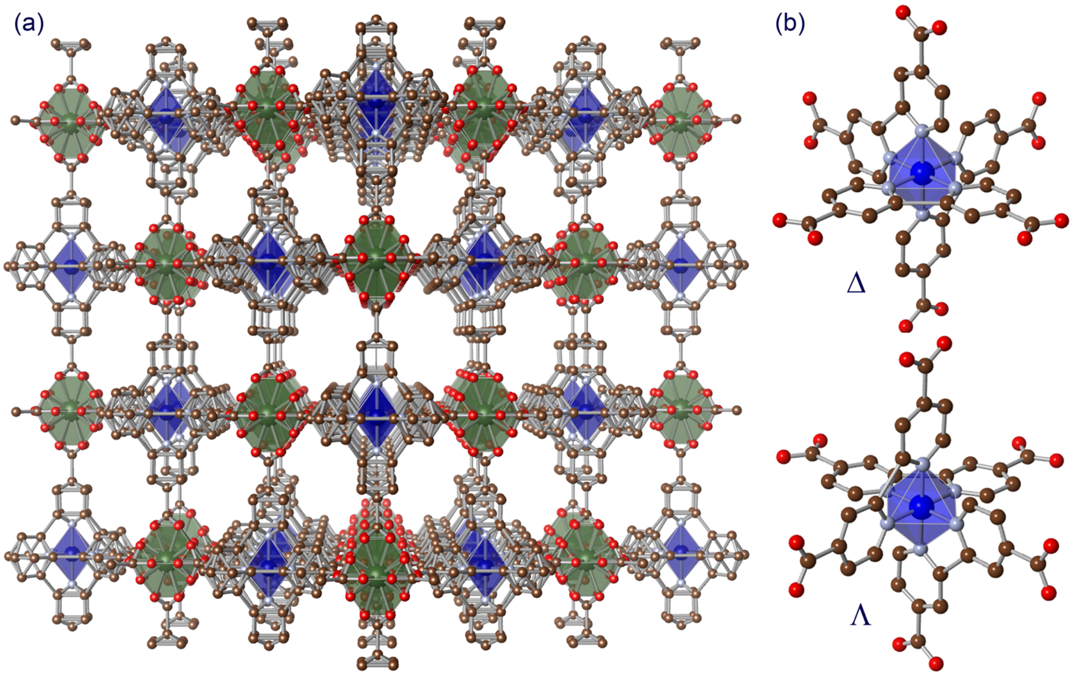

**Figure 2.** (a) Packing diagrams of **Er−Co** PCP viewed along the *a* + *b* axis. (b) Disordered model of Δ- and Λ-$[Co(dcbpy)_3]^{3-}$ at one Co(III) site. Coordination spheres of Co(III) and Er(III) ions are shown as blue and dark-green polyhedrons, respectively. Brown, light blue, and red balls represent C, N, and O atoms, respectively. Noncoordinated water molecules and H atoms are omitted for clarity.

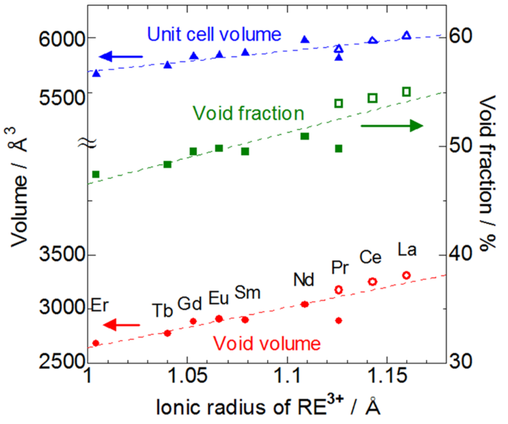

**Figure 3.** Plots of the unit cell volume, void volume (Å$^3$), and void fraction (%) against the ionic radius (Å) of the 8-coordinated RE$^{3+}$ ion. Open and closed symbols indicate the data of orthorhombic and cubic structures, respectively. Unit cell and void volumes of orthorhombic **RE−Co** PCPs ($Z$ = 16) are normalized to compare the data for cubic **RE−Co** PCPs ($Z$ = 4). Dashed lines are drawn as a guide.

enantiomers. However, the average **Gd−O** distance agreed well with the sum of the ionic radii of Gd$^{3+}$ and O$^{2-}$ (see Table 2). This agreement would enhance the thermodynamic stability of the guest-adsorbed porous structure of **Gd−Co**, resulting in the clear transition behavior.

In order to further investigate the guest-induced amorphous−crystalline transition, vapor-adsorption isotherms of **La−Co**, **Gd−Co**, and **Er−Co** PCPs were performed. All samples were dried overnight at 373 K under vacuum prior to the measurements, and all crystal water molecules in the porous channels were confirmed to be removed by the weight change of each sample before and after this drying process. Figure 5a shows the water-vapor-adsorption isotherms of the **RE−Co** PCPs at 298 K. As expected from the porous structures and changes of PXRD patterns, these PCPs commonly showed the isotherms with large hysteresis between the adsorption and the desorption processes, which is a characteristic feature of vapor adsorption involving a structural transition of the framework. In addition, $N_2$ adsorption isotherms of **RE−Co** at 77 K revealed that the dried amorphous phase is nonporous (see Figure S6, Supporting Information). In the low vapor pressure region (below 0.1 $P/P_0$), the amount of water vapor uptake by the three **RE−Co** sharply increased above 4 mol·mol$^{-1}$, suggesting the high hydrophilicity of pores of **RE−Co** frameworks as expected from the crystal structures. On the other hand, in the high vapor pressure region (above 0.4 $P/P_0$), the amounts of cubic **Gd−Co** and **Er−Co** PCPs monotonically and quasi-linearly increased whereas the rate of water vapor uptake of **La−Co** increased remarkably. The difference probably originates from the pore character; the orthorhombic **La−Co** PCP has three different kinds of pore channels (as discussed in the Crystal Structures of RE−Co PCPs section), but the other cubic **RE−Co** have only one kind of porous channel because of the structural disorder of the two enantiomers of $[Co(dcbpy)_3]^{3-}$ metalloligand. The two largest porous channels (with >6 Å diameter) of **La−Co** may enable the adsorption of water molecules by bilayer adsorption in the higher vapor pressure region, as the multilayer adsorption is typically observed for mesoporous materials. In contrast, such bilayer adsorption would be suppressed in cubic **RE−Co** PCPs by the structural disorder of Δ- and Λ-$[Co(dcbpy)_3]^{3-}$. The saturated amounts of the water-vapor adsorption were estimated to be 17.4, 13.8, and 15.9 mol·mol$^{-1}$ for **La−Co**, **Gd−Co**, and **Er−Co**, respectively. The saturated amount of adsorbed water for **Er−Co** was marginally larger than for **Gd−Co**, in spite of the smaller void fraction (49.5% for **Gd−Co** and 47.4% for **Er−Co**). This inverted order could be related to the difference in pore diameter between **Er−Co** and **Gd−Co**. In the smaller pore of **Er−Co**, host−guest interaction (i.e., electrostatic and

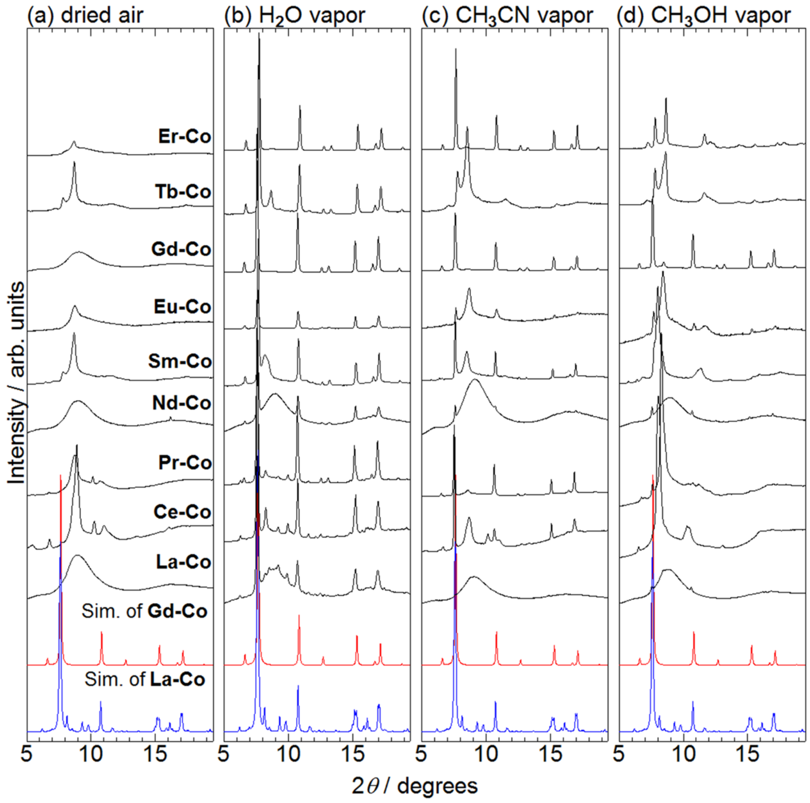

**Figure 4.** PXRD patterns [$\lambda$ = 1.200(1) Å] of **RE−Co** PCPs under exposure to (a) dried air, (b) $H_2O$ vapor, (c) $CH_3CN$ vapor, and (d) $CH_3OH$ vapor at room temperature. Blue and red lines at the bottoms are the simulation patterns calculated from the crystal structures of **La−Co** and **Gd−Co**, respectively.

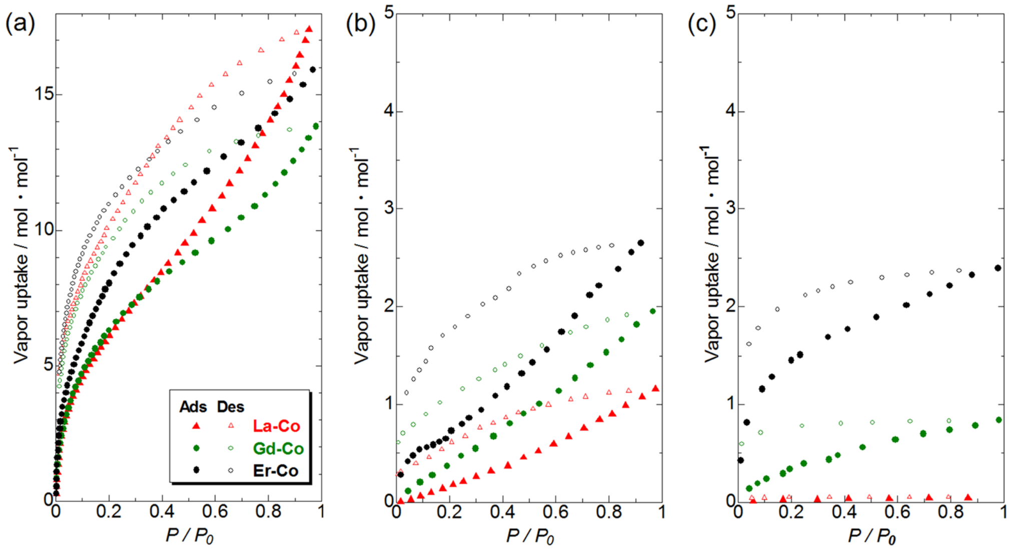

**Figure 5.** (a) $H_2O$-, (b) $CH_3CN$-, and (c) $CH_3OH$-vapor-adsorption isotherms for orthorhombic **La−Co**, cubic **Gd−Co**, and cubic **Er−Co** (red triangle, green circle, and black circle) PCPs at 298 K. Closed and open symbols show the adsorption and desorption processes, respectively.

van der Waals interactions) between the porous framework of **Er−Co** and water molecules would be more effective than that in **Gd−Co**. In fact, the vapor uptake of **Er−Co** in the low vapor pressure region (below 0.2 $P/P_0$) increased more sharply than for the other two. More drastic differences were observed in the $CH_3CN$- and $CH_3OH$-vapor-adsorption isotherms, as shown in Figure 5b and 5c. Only the **Er−Co** PCP showed a sharp increase in vapor uptake in the low vapor pressure region (<0.1 $P/P_0$) for both vapor-adsorption isotherms, suggesting that the host−guest interaction in the **Er−Co** framework would be more effective than the other two **RE−Co**. The saturated amounts of adsorbed $CH_3CN$ were 1.16, 1.95, and 2.65 mol·mol$^{-1}$ for **La−Co**, **Gd−Co**, and **Er−Co**, respectively, which was remarkably smaller than those for water vapor. The $CH_3OH$ vapor uptakes of **Gd−Co** and **Er−Co** under the saturated vapor pressure (0.84 and 2.40 mol·mol$^{-1}$, respectively) were found to be about one-half of those for $CH_3CN$ vapor, whereas the **La−Co** did not adsorb $CH_3OH$ vapor at all. Although the

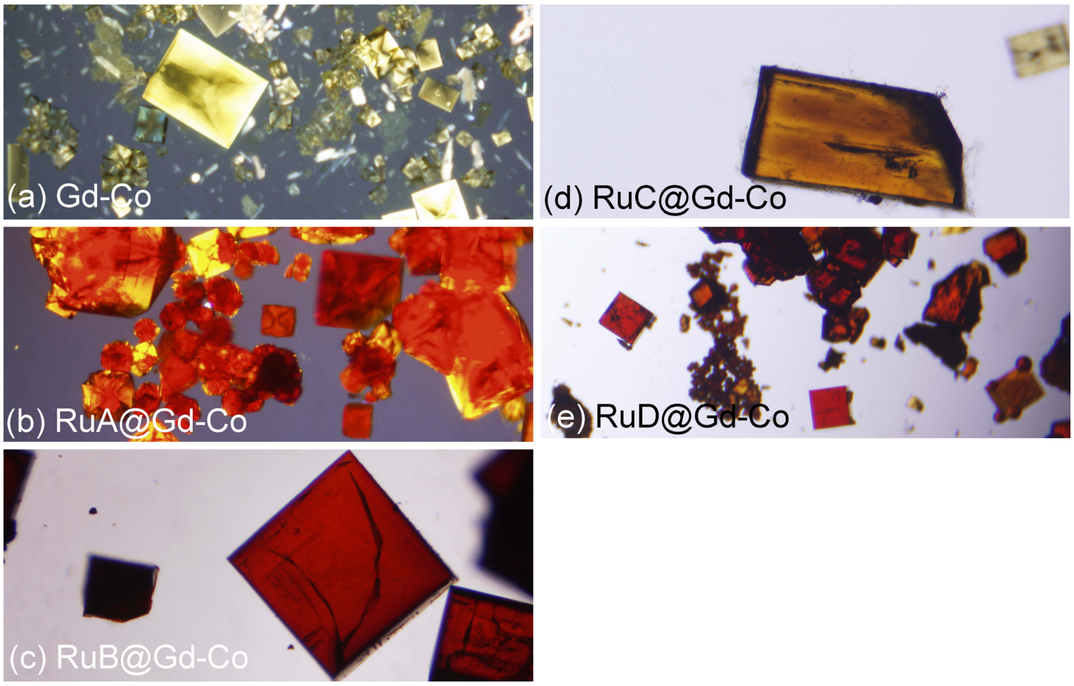

**Figure 6.** Photographs of (a) nondoped **Gd−Co**, (b) ***Ru*A@Gd−Co**, (c) ***Ru*B@Gd−Co**, (d) ***Ru*C@Gd−Co**, and (e) ***Ru*D@Gd−Co**.

order of the saturated amounts was contrary to the order of the void fraction, the vapor-induced amorphous−crystalline transitions of **Gd−Co** and **Er−Co** could possibly be the origin of higher vapor uptakes than that for **La−Co**. The PXRD patterns of **Gd−Co** and **Er−Co** clearly indicate that their porous frameworks were regenerated under exposure to $CH_3CN$ vapor, whereas the amorphous-like PXRD pattern of **La−Co** was hardly changed, as shown in Figure 4c. Under $CH_3OH$ vapor, the **Gd−Co** showed almost identical PXRD patterns to the simulation, whereas the pattern of **Er−Co** was different from the simulation of isomorphic **Gd−Co** (Figure 4d), indicating that the structure of the $CH_3OH$-adsorbed phase of **Er−Co** should be different from that of water and $CH_3CN$ vapors. However, in both cases, the adsorption of hydrophilic small molecules such as water and $CH_3CN$ is one of the most effective driving forces to transform the **RE−Co** to vapor-absorbable frameworks from the amorphous-like solid. The reason why the framework of **La−Co** was not regenerated under exposure to $CH_3CN$ or $CH_3OH$ vapor could be that it has a larger pore diameter than the other two; hence, a larger amount of adsorption would be required for regeneration of the porous framework of **La−Co** than for those of **Gd−Co** or **Er−Co**. In fact, for the water-vapor-induced amorphous−crystalline transitions, the porous frameworks of **Gd−Co** and **Er−Co** began to regenerate at a lower relative humidity (43% and 23% RH, respectively), but higher RH was required for **La−Co** (almost 100% RH, see Figure S7, Supporting Information).

**Ru(II)−Metalloligand Doping Into the Gd−Co Framework.** As mentioned in the Introduction, utilization of the metalloligand to incorporate an additional function to flexible porous coordination polymers is one of the most powerful methods to create multifunctional porous materials.[39−41] From this point of view, doping (= mixing) of a different metalloligand into the **Co** site of a **RE−Co** PCP framework could be an additional and effective method to modulate the guest-adsorption behaviors. Herein, in order to clarify the structural requirement for the metalloligand dopant to achieve effective incorporation in the PCP framework, we discuss the effect of doping of four different Ru(II)−metalloligands, $[Ru(H_2dcbpy)(Hdcbpy)_2]$, $[Ru(H_2dcbpy)_2Cl_2]$, $[Ru(H_2dcbpy)(tpy)Cl]Cl$, and $[Ru(H_2dcbpy)(H_2dctpy)Cl]Cl$ (abbreviated as ***Ru*A**, ***Ru*B**, ***Ru*C**, and ***Ru*D**, respectively), into the **Gd−Co** framework.

The doping of Ru(II)−metalloligands into the **Gd−Co** framework was conducted by diffusion of $GdCl_3$ in ethanol solution into the aqueous solution of $[Co(dcbpy)_3]^{3-}$ (abbreviated as **Co**) mixed with Ru(II)−metalloligand (the mixing molar ratio of **Co**:***Ru*X** is 8:2, see the Experimental Section). LiCl (ca. 10 equiv tofo $GdCl_3$) was added to the aqueous solution of the metalloligand in order to compensate for the different charge between **Co** and ***Ru*X**. As shown in Figure 6, the obtained single crystals of Ru(II)−metalloligand-doped ***Ru*A@Gd−Co**, ***Ru*B@Gd−Co**, and ***Ru*D@Gd−Co** uniformly showed reddish-orange color, different from the yellow-colored nondoped **Gd−Co**, implying that ***Ru*A**, ***Ru*B**, and ***Ru*D** were incorporated into the **Gd−Co** framework. In contrast, the crystal color of ***Ru*C@Gd−Co** was found to be brown-yellow, which is similar to the yellow color of nondoped **Gd−Co** rather than the reddish-orange Ru(II)-doped ones, implying that the ***Ru*C** dopant bearing a lower number of coordinating carboxylates than the parent Co(III)−metalloligand is hardly incorporated into the **Gd−Co** framework. Next, we conducted ICP-AES analysis to evaluate the Ru(II)−dopant concentration in each ***Ru*X@Gd−Co** framework (see Table 4). As expected from the structural similarity between **Co** and ***Ru*A**, the molar ratio of ***Ru*A** to ***Co*** of ***Ru*A@Cd−Co** was found to be 0.212:0.788, which is in agreement with the mixing ratio in the synthesis. In contrast, the molar ratios of ***Ru*X** to **Co** of the other three ***Ru*X@Gd−Co** were found to be lower than the mixing ratio in the synthesis. This difference obviously suggests that the structural similarity between the dopant and the parent metalloligand is important. It may be interesting to note that the molar ratios of ***Ru*X** to **Co** of ***Ru*B@Gd−Co** and ***Ru*D@Gd−Co** were slightly larger than that of ***Ru*C@Gd−Co**, suggesting that the larger number of coordination sites and/or

**Table 4. Structural Parameters of *Ru*X Dopant and Estimated Molar Ratio of Co to *Ru*X in *Ru*X@Gd−Co by ICP-AES Analysis**

| complex | *Ru*X dopant | no. of COOH in *Ru*X | molecular charge | Co (mol %) | *Ru*X (mol %) |
|---|---|---|---|---|---|
| ***Ru*A@Gd−Co** | $[Ru(dcbpy)_3]^{4-}$ | 6 | 4− | 0.788 | 0.212 |
| ***Ru*B@Gd−Co** | $[Ru(dcbpy)_2Cl_2]^{4-}$ | 4 | 4− | 0.947 | 0.053 |
| ***Ru*C@Gd−Co** | $[Ru(dcbpy)(tpy)Cl]^{-}$ | 2 | 1− | 0.966 | 0.034 |
| ***Ru*D@Gd−Co** | $[Ru(dcbpy)(dctpy)Cl]^{3-}$ | 4 | 3− | 0.928 | 0.072 |

the molecular charge in the ***Ru*B** and ***Ru*D** dopants is an important factor to incorporate more effectively into the **Gd−Co** framework.

In order to check the uniformity of **RuX** in the ***Ru*X@Gd−Co** crystals, scanning electron microscopy with energy-dispersive X-ray spectroscopy (SEM-EDS) measurement was conducted. In the SEM-EDS elemental mapping of the non-doped **Gd−Co** crystal, negligibly small contrast corresponding to the boundary between the **Gd−Co** crystal and the background (carbon tape) was not observed in the Ru L-edge region, as shown in Figure 7a, corresponding to the absence of ***Ru*X**. In contrast, a sharp contrast in the Ru L-edge region was obviously observed for ***Ru*A@Gd−Co** crystal (Figure 7d), as well as in the other Gd L-edge and Co K-edge regions (Figure 7e and 7f), clearly indicating that the ***Ru*A** exists uniformly in the ***Ru*A@Gd−Co**. On the other hand, the similar but unclear contrasts in the Ru L-edge region were observed for the other three ***Ru*X@Gd−Co**, being consistent with the lower concentration of the ***Ru*X** dopant in the **Gd−Co** framework as estimated from the ICP-AES analysis.

In order to clarify the existence of ***Ru*X** dopant in the **Gd−Co** framework, UV−vis diffuse reflectance spectra of these ***Ru*X@Gd−Co** were measured in the solid state, because these Ru(II) complexes are well known to exhibit a strong MLCT transition in the visible region.[43] As shown in Figure 8, MLCT transitions originated from the ***Ru*A** and ***Ru*D** dopants were clearly observed at 475 and 465 nm in the UV−vis diffuse reflectance spectrum of ***Ru*A@Gd−Co** and ***Ru*D@Gd−Co** (Figure 8a and 8d), respectively, suggesting that these ***Ru*X** dopants were certainly incorporated into the **Gd−Co** framework. Although a similar absorption band was also observed for ***Ru*B@Gd−Co**, the band was significantly shifted to longer wavelength by about 60 nm than that of ***Ru*B** dopant. This absorption band shift suggests that the ***Ru*B** dopant was incorporated into the **Gd−Co** framework, but the molecular structure would be changed in the synthesis. In fact, we observed that the $^1H$ NMR spectrum of ***Ru*B** dopant in basic aqueous solution, which is a similar condition in the synthesis, was gradually changed to the spectrum assignable to that of the Ru(II) complex with two aqua ligands instead of two $Cl^-$ ligands of ***Ru*B** (see Figure S8, Supporting Information). On the other hand, the observed spectrum for ***Ru*C@Gd−Co** was found to be almost identical to that of nondoped **Gd−Co**, indicating that the ***Ru*C** dopant was hardly incorporated into the **Gd−Co** framework.

Further identification of these ***Ru*X@Gd−Co** was conducted by PXRD measurement to evaluate the doping effect of ***Ru*X** into the **Gd−Co** framework (see Figure S9, Supporting Information). In addition to nondoped **Gd−Co**, obtained PXRD patterns of ***Ru*X@Gd−Co** were featureless and broad, but under exposure to water vapor, it changed to the diffraction pattern almost identical to the simulation based on the crystal structure of **Gd−Co**. Thus, this result indicates that the overall structural feature of the porous framework of **Gd−Co** including the amorphous−crystalline structural transition behavior triggered by water-vapor adsorption/desorption was not changed by the ***Ru*X** doping. The observed patterns being identical to the **Gd−Co** simulation also suggests that the ***Ru*X** dopants themselves did not form any crystalline impurities composed of $Gd^{3+}$ cation and ***Ru*X**.

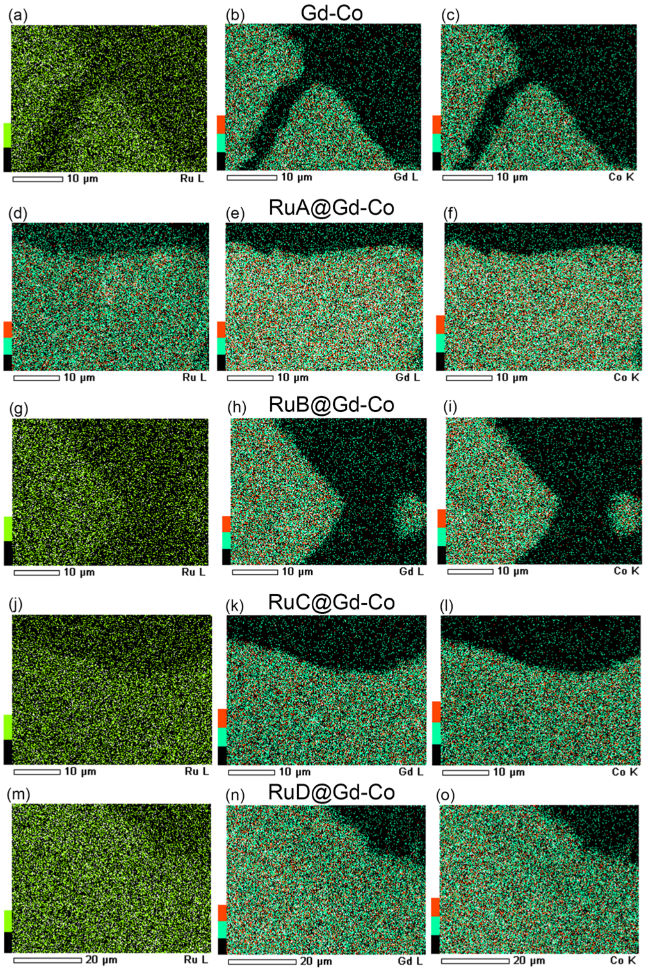

**Figure 7.** SEM-EDS elemental mapping at (a, d, g, j, m) Ru L-edge, (b, e, h, k, n) Gd L-edge, and (c, f, i, l, o) Co K-edge regions for nondoped **Gd−Co** (a−c), ***Ru*A@Gd−Co** (d−f), ***Ru*B@Gd−Co** (g−i), ***Ru*C@Gd−Co** (j−l), and ***Ru*D@Gd−Co** (m−o).

The range of analyses for ***Ru*X@Gd−Co**, mentioned above, clearly indicates that the dopant concentration in the ***Ru*X**-doped **Gd−Co**, ***Ru*X@Gd−Co** significantly depends on the molecular structure of the ***Ru*X** dopant. The isostructural ***Ru*A** dopant with the parent metalloligand **Co** was uniformly incorporated into the **Gd−Co** framework, and the dopant concentration was found to agree well with the concentration in the synthesis. On the other hand, the ***Ru*X** dopant concentrations in ***Ru*B@Gd−Co** and ***Ru*D@Gd−Co** were lower than that in ***Ru*A@Gd−Co**, and the ***Ru*C** dopant was found to be hardly incorporated into the **Gd−Co** framework. These differences should be originated from the molecular structural similarity between the parent **Co** and the ***Ru*X** dopant, i.e., the lattice distortion derived from the doping of isostructural ***Ru*A** with **Co** would be negligibly small. As a result, the molar ratio

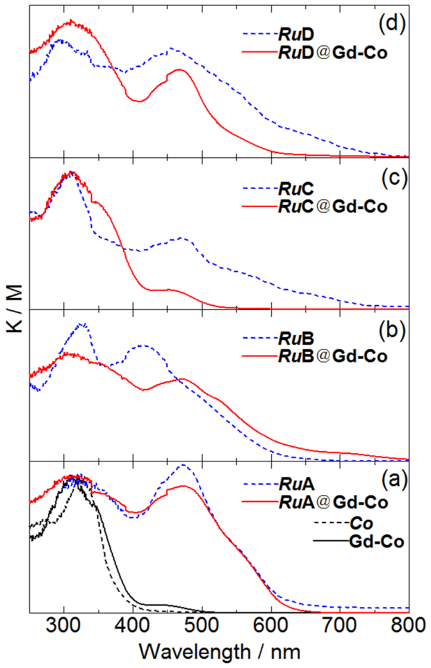

**Figure 8.** UV−vis diffuse reflectance spectra of (a) ***Ru*A@Gd−Co**, (b) ***Ru*B@Gd−Co**, (c) ***Ru*C@Gd−Co**, and (d) ***Ru*D@Gd−Co** in the solid states. Black solid and broken lines in (a) show the spectra of the parent Co(III)−metalloligand **Co** and nondoped **Gd−Co**. Each spectrum of ***Ru*X** dopant in the solid state is shown by the blue broken line.

of ***Ru*A** to **Co** in ***Ru*A@Gd−Co** agrees well with the ratio in the synthesis. In addition, in our preliminary results on the syntheses of the more heavily ***Ru*A**-doped **Gd−Co**, the upper limit of the concentration of ***Ru*A** in ***Ru*A@Gd−Co** would be around 50%, as suggested by PXRD and ICP-AES measurements (see Figure S10 and Table S1, Supporting Information). On the other hand, ***Ru*B** and ***Ru*D** dopants have four $COO^-$ coordination sites in their ligands which enable them to be incorporated into the **Gd−Co** framework, but the lattice distortion triggered by ***Ru*B** and ***Ru*D** doping should be larger than that by ***Ru*A**, resulting in the lower concentration of ***Ru*X** dopant in the **Gd−Co**. The reason why the ***Ru*C** dopant was hardly incorporated would be due to the lower number of coordination sites and/or smaller ionic charge than that of ***Ru*A**.

**Vapor-Adsorption Isotherms of the Ru(II)−Metalloligand-Doped Gd−Co Framework.** We successfully synthesized the ***Ru*A**-doped **Gd−Co** framework with a relatively high concentration (≅20 mol % **Co** was replaced by ***Ru*A**), ***Ru*A@Gd−Co**, and various measurements revealed that the ***Ru*A** dopant uniformly incorporated. However, these measurements did not reveal the location and local structure of dopant in the framework. Considering the fact that the ***Ru*A** dopant has almost the same molecular structure with that of the **Co**, one plausible case is that the ***Ru*A** dopant was incorporated by exchange with the **Co** site in the porous framework. In this case, incorporation of an additional cation (probably $Li^+$, as suggested by ICP-AES analysis mentioned above) should be involved to compensate for the different molecular charges between **Co** and ***Ru*A**, which should have an effect on the vapor-adsorption property of **Gd−Co**. Thus, we measured several kinds of vapor-adsorption isotherms in order to estimate the effect of ***Ru*A** doping into the **Gd−Co** porous framework. Figure 9 shows the $H_2O$-, $CH_3CN$-, and $CH_3OH$-vapor-adsorption isotherms of ***Ru*A@Gd−Co** in comparison with those of nondoped **Gd−Co**. The observed vapor-adsorption isotherms of ***Ru*A@Gd−Co** for these vapors were similar to those of nondoped **Gd−Co**, but several noteworthy differences were also observed. The first difference is in the amount of vapor uptake under saturated conditions; the amounts of water and $CH_3CN$ vapors taken up by ***Ru*A@Gd−Co** (10.4 and 1.47 mol·mol$^{-1}$, see Figures 9a and 9b) were found to be about 75% of the amounts for nondoped **Gd−Co** (13.8 and 1.95 mol·mol$^{-1}$), whereas the amount for $CH_3OH$ vapor was not influenced by the ***Ru*A** doping (see Figure 9c).

The second difference is regarding the adsorption behavior; the amounts of adsorption for ***Ru*A@Gd−Co** for water vapor increased more sharply in the low vapor pressure region of 0.2−0.3 $P/P_0$ than that for **Gd−Co**, while the amount for $CH_3CN$ vapor for ***Ru*A@Gd−Co** increased more slowly than that for **Gd−Co** with increasing vapor pressure.

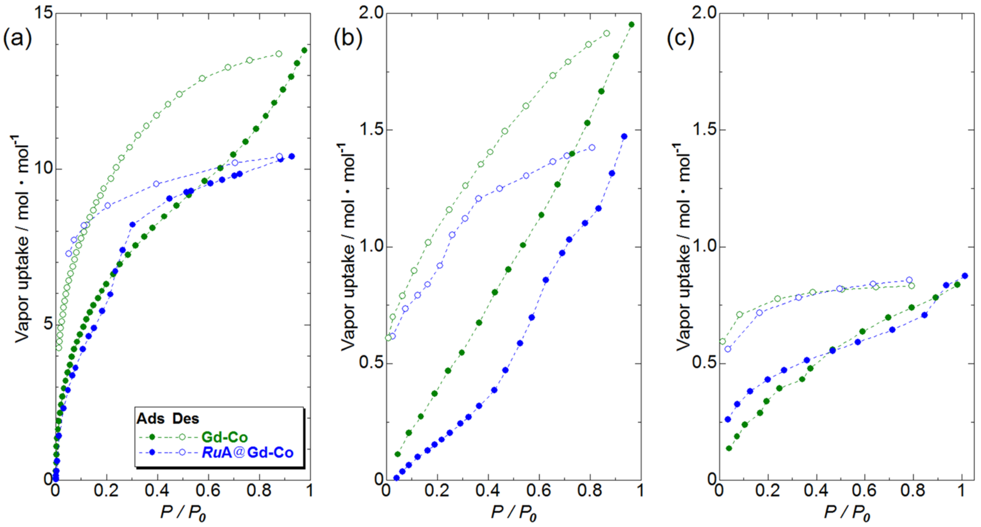

**Figure 9.** (a) $H_2O$- (b) $CH_3CN$-, and (c) $CH_3OH$-vapor-adsorption isotherms of ***Ru*A@Gd−Co** PCPs (blue circles) at 298 K in comparison with those of nondoped **Gd−Co** PCPs (green circles, same data shown in Figure 5). Closed and open symbols show the adsorption and desorption processes, respectively.

Considering the fact that the crystal structure of ***Ru*A@Gd−Co** is almost identical to that of nondoped **Gd−Co** except for the existence of the ***Ru*A** dopant, the observed differences in the vapor-adsorption isotherms mentioned above should be due to the doping of ***Ru***. The origin of the lower water and $CH_3CN$ vapor uptakes of ***Ru*A@Gd−Co** under saturated vapor pressure conditions than those of **Gd−Co** is probably the occupation of the void space of the **Gd−Co** framework by $Li^+$ cations, which decreases the solvent-accessible void space. In fact, atomic emission from the Li element was also observed for ***Ru*A@Cd−Co** in the ICP-AES spectrum, suggesting that the $Li^+$ cation was certainly incorporated into the porous channel of **Gd−Co**, probably owing to the charge compensation of the ***Ru*A** dopant. In addition, we also checked SEM-EDS analysis for the ***Ru*A@Gd−Co** synthesized in the 10 equiv of NaCl (instead of LiCl) containing aqueous solution and found that $Na^+$ cations were incorporated uniformly in the ***Ru*A@Gd−Co** framework (see Figure S11, Supporting Information). Thus, the larger amount of adsorption for both water and $CH_3OH$ vapor for ***Ru*A@Gd−Co** than that for **Gd−Co** in the low vapor pressure region is due to the existence of the $Li^+$ cation in the porous channel, because $Li^+$ has the largest hydration enthalpy (503 $kJ\cdot mol^{-1}$) among the monocationic metal ions.[80] Such a large hydration enthalpy could enhance the interaction between the porous framework of ***Ru*A@Gd−Co** and water or $CH_3OH$, resulting in the sharp increase in the amount of adsorption in the lower vapor pressure regions. Comparable adsorption amounts of $CH_3OH$ vapor for ***Ru*A@Gd−Co** with that of **Gd−Co**, in spite of the occupation of the void space by $Li^+$ cations, may also result from the adsorption enhancement due to the coordination of adsorbed $CH_3OH$ molecules to $Li^+$ ions. Conversely, $CH_3CN$ vapor adsorption into the porous framework of **Gd−Co** in the low vapor pressure region (below 0.4 $P/P_0$) seems to be suppressed by the ***Ru*A** doping. From the viewpoint of electrostatic interaction, the ***Ru*A** doping into the **Gd−Co** framework may stabilize the nonporous amorphous phase, because the electrostatic interaction between the incorporated $Li^+$ cation in the pore and the negatively charged ***Ru*A** dopant in the framework would be more effective in the amorphous (pore-collapsed) phase than that in the porous phase. As a result, adsorption of polar but proton-accepting $CH_3CN$ vapor into the ***Ru*A@Gd−Co** framework would be suppressed in the low vapor pressure region by the tightly packed structure.

## ■ CONCLUSION

We systematically synthesized new flexible porous coordination polymers **RE−Co** composed of Co(III)−metalloligand $[Co(dcbpy)_3]^{3-}$ (**Co**) and a series of lanthanide ions ($La^{3+}$, $Ce^{3+}$, $Pr^{3+}$, $Nd^{3+}$, $Sm^{3+}$, $Eu^{3+}$, $Gd^{3+}$, $Tb^{3+}$, $Er^{3+}$). Single-crystal X-ray structural analysis clearly revealed that the **RE−Co** PCPs commonly had rock-salt-type porous frameworks built from Co(III)−metalloligand and the $RE^{3+}$ ion and that the porosity of the **RE−Co** can be controlled by changing the $RE^{3+}$ ion from 47.4% (**Er−Co**) to 55.0% (**La−Co**). The two enantiomers of $[Co(dcbpy)_3]^{3-}$, Δ- and Λ-$[Co(dcbpy)_3]^{3-}$, were disordered at the one $[Co(dcbpy)_3]^{3-}$ site in the **RE−Co** PCPs with smaller and heavier $RE^{3+}$ ions than $Pr^{3+}$, whereas they were completely ordered at different sites in the **RE−Co** PCPs with larger $RE^{3+}$ ions, probably because of the 10-coordinated bicapped square-antiprism structure of the $RE^{3+}$ ion. Vapor-adsorption properties of **RE−Co** PCPs also strongly depend on the kind of $RE^{3+}$ ion. Although the **RE−Co** PCPs can commonly adsorb large amounts of water vapor, at least 13 $mol\cdot mol^{-1}$ by involving the amorphous−crystalline transition, the **Er−Co** PCPs with the smallest void fraction in the series adsorbed a larger amount of $CH_3CN$ and $CH_3OH$ vapors than the other **RE−Co** PCPs, suggesting that the host−guest interaction would be enhanced in the smaller pore channels in **Er−Co**. To further tune the guest-adsorption behavior of the **Gd−Co** framework, the doping of four different Ru(II)−metalloligands, $[Ru(H_2dcbpy)(Hdcbpy)_2]$, $[Ru(H_2dcbpy)_2Cl_2]$, $[Ru(H_2dcbpy)(tpy)Cl]Cl$, and $[Ru(H_2dcbpy)(H_2dctpy)Cl]Cl$ (abbreviated as ***Ru*A**, ***Ru*B**, ***Ru*C**, and ***Ru*D**, respectively), has been conducted. ICP-AES, SEM-EDS, UV−vis, and PXRD analyses indicate that the ***Ru*A**, ***Ru*B**, and ***Ru*D** dopants with lots of coordinating $COO^-$ groups were successfully incorporated into the **Gd−Co** framework uniformly and randomly by replacing the **Co** metalloligand site, whereas the ***Ru*C** dopant was hardly incorporated probably owing to lower number of coordinating $COO^-$ groups and/or smaller molecular charge than the other dopant. The dopant concentration in **Gd−Co** was found to strongly depend on the structural similarity between the parent **Co** and the dopant. The $Li^+$ cation was simultaneously incorporated as the countercation into the porous channels of ***Ru*A@Gd−Co** to compensate for the metalloligand ***Ru*A**, which is more negatively charged than **Co**. The Ru(II)-doped ***Ru*A@Gd−Co** adsorbed water vapor more effectively in the low vapor pressure region than that of the nondoped **Gd−Co**, whereas the $CH_3CN$ adsorption of ***Ru*A@Gd−Co** was suppressed in the low vapor pressure region, below 0.3 $P/P_0$. These differences could be due to the enhancement of the electrostatic interaction between the highly polar guest molecule and the porous host framework by the more negatively charged ***Ru*A** and counter $Li^+$ cations. Our findings about the sensitivity of the molecular structure of the dopant in the metalloligand doping technique could be beneficial for construction of a multifunctional PCP system whose properties are derived from the cooperative phenomena of two or more functional building blocks. Further study on the development of new multifunctional PCPs based on the metalloligand-doping technique is now in progress.

## ■ ASSOCIATED CONTENT

### Ⓢ Supporting Information

X-ray crystallographic data in CIF format of **Ce−Co**, **Pr−Co**, **Sm−Co**, **Eu−Co**, **Tb−Co**, **Er−Co**; IR spectra of **RE−Co**; TG analysis of **Pr−Co**; PXRD patterns of as-synthesized **La−Co** and **Er−Co**; PXRD patterns of the **Pr−Co** and **Eu−Co** PCPs under exposure to various organic vapors; $N_2$ adsorption isotherms of **Nd−Co** and **Er−Co** at 77 K; RH dependence of PXRD patterns of **La−Co**, **Gd−Co**, and **Er−Co** PCPs at room temperature; $^1H$ NMR spectral change of ***Ru*B** dopant; PXRD patterns of ***Ru*X@Gd−Co** (X = A, B and D) under exposure to dried air and saturated water vapor; PXRD patterns and ICP-AES results of ***Ru*A@Gd−Co** with the various **RuA**-doping levels; SEM-EDS images of ***Ru*A@Gd−Co** obtained from the reaction solution in the presence of 10 equiv of NaCl instead of LiCl. This material is available free of charge via the Internet at http://pubs.acs.org.

## ■ AUTHOR INFORMATION

### Corresponding Authors

*E-mail: akoba@sci.hokudai.ac.jp.
*E-mail: mkato@sci.hokudai.ac.jp.

### Author Contributions

The manuscript was written through contributions of all authors. All authors have given approval to the final version of the manuscript.

### Notes

The authors declare no competing financial interest.

## ■ ACKNOWLEDGMENTS

This work was supported by JST-PRESTO, Grant-in-Aid for Scientific Research (B) (23350025), (C) (26410063), Coordination Programming (No. 2107), Artificial Photosynthesis (No. 2406), Young Scientists (B) (24750049), the Global COE Program (Project No. B01: Catalysis as the Basis for Innovation in Materials Science) from MEXT, Japan.

## ■ REFERENCES

(1) In *Porous Materials*; Bruce, D. W., O'Hare, D., Walton, R. I., Eds.; John Wiley & Sons: Chichester, 2011.

(2) Li, H.; Eddaoudi, M.; O'Keeffe, M.; Yaghi, O. M. *Nature* **1999**, *402*, 276−279.

(3) Yaghi, O. M.; O'Keeffe, M.; Ockwig, N. W.; Chae, H. K.; Eddaoudi, M.; Kim, J. *Nature* **2003**, *423*, 705−714.

(4) Kitagawa, S.; Kondo, M. *Bull. Chem. Soc. Jpn.* **1998**, *71*, 1739−1753.

(5) Kitagawa, S.; Kitaura, R.; Noro, S. *Angew. Chem., Int. Ed.* **2004**, *43*, 2334−2375.

(6) Uemura, K.; Kitagawa, S.; Kondo, M.; Fukui, K.; Kitaura, R.; Chang, H.-C.; Mizutani, T. *Chem.—Eur. J.* **2002**, *8*, 3586−3600.

(7) Matsuda, R.; Kitaura, R.; Kitagawa, S.; Kubota, Y.; Belosludov, R. V.; Kobayashi, T. C.; Sakamoto, H.; Chiba, T.; Takata, M.; Kawazoe, Y.; Mita, Y. *Nature* **2005**, *436*, 238−241.

(8) Dincă, M.; Long, J. R. *J. Am. Chem. Soc.* **2005**, *127*, 9376−9377.

(9) Horike, S.; Tanaka, D.; Nakagawa, K.; Kitagawa, S. *Chem. Commun.* **2007**, 3395−3397.

(10) Zou, Y.; Hong, S.; Park, M.; Chun, H.; Lah, M. S. *Chem. Commun.* **2007**, 5182−5184.

(11) Serre, C.; Bourrelly, S.; Vimont, A.; Ramsahye, A. A.; Maurin, G.; Llewellyn, P. L.; Daturi, M.; Filinchuk, Y.; Leynaud, O.; Barnes, P.; Férey, G. *Adv. Funct. Mater.* **2007**, *19*, 2246−2251.

(12) Tanaka, D.; Nakagawa, K.; Higuchi, M.; Horike, S.; Kubota, Y.; Kobayashi, T. C.; Takata, M.; Kitagawa, S. *Angew. Chem., Int. Ed.* **2008**, *47*, 3914−3918.

(13) Li, J.-R.; Kuppler, R. J.; Zhou, H.-C. *Chem. Soc. Rev.* **2009**, *38*, 1477−1504.

(14) Horike, S.; Shimomura, S.; Kitagawa, S. *Nat. Chem.* **2009**, *1*, 695−704.

(15) Li, J.-R.; Huppler, R. J.; Zhou, H.-C. *Chem. Soc. Rev.* **2009**, *38*, 1477−1504.

(16) Noro, S.; Akutagawa, T.; Nakamura, T. *Chem. Commun.* **2010**, *46*, 1334−3136.

(17) Chen, B.; Xiang, S.; Qian, G. *Acc. Chem. Res.* **2010**, *43*, 1115−1124.

(18) Bae, Y.-S.; Snurr, R. Q. *Angew. Chem., Int. Ed.* **2011**, *50*, 11586−11596.

(19) Farha, O. K.; Eryazici, I.; Jeong, N. C.; Hauser, B. G.; Wilmer, C. E.; Sarjeant, A. A.; Snurr, R. Q.; Nguyen, S. T.; Yazaydin, A. Ö.; Hupp, J. T. *J. Am. Chem. Soc.* **2012**, *134*, 15016−15021.

(20) Furukawa, H.; Cordova, K. E.; O'Keeffe, M.; Yaghi, O. M. *Science* **2013**, *341*, 1230444.

(21) Li, L.; Tang, S.; Wang, C.; Lv, X.; Jiang, M.; Wu, H.; Zhao, X. *Chem. Commun.* **2014**, *50*, 2304−2307.

(22) Dybtsev, D. N.; Nuzhdin, A. L.; Chun, H.; Bryliakov, K. P.; Talsi, E. P.; Fedin, V. P.; Kim, K. *Angew. Chem., Int. Ed.* **2006**, *45*, 916−920.

(23) Shultz, A. M.; Farha, O. K.; Hupp, J. T.; Nguyen, S. T. *J. Am. Chem. Soc.* **2009**, *131*, 4204−4205.

(24) Yang, L.; Kinoshita, S.; Yamada, T.; Kanda, S.; Kitagawa, H.; Tokunaga, M.; Ishimoto, T.; Ogura, T.; Nagumo, R.; Miyamoto, A.; Koyama, M. *Angew. Chem., Int. Ed.* **2010**, *49*, 5348−5351.

(25) Halder, G. J.; Kepert, C. J.; Moubaraki, B.; Murray, K. S.; Cashion, J. D. *Science* **2002**, *298*, 1762−1765.

(26) Kim, H.; Samsonenko, D. G.; Yoon, M.; Yoon, J. W.; Hwang, Y. K.; Chang, J.-S.; Kim, K. *Chem. Commun.* **2008**, 4697−4699.

(27) An, J.; Geib, S. J.; Rosi, N. L. *J. Am. Chem. Soc.* **2009**, *131*, 8376−8377.

(28) Sato, H.; Matsuda, R.; Sugimoto, K.; Takata, M.; Kitagawa, S. *Nat. Mater.* **2010**, *9*, 661−666.

(29) Wu, C.-D.; Hu, A.; Zhang, L.; Lin, W. *J. Am. Chem. Soc.* **2005**, *127*, 8940−8941.

(30) Doonan, C. J.; Morris, W.; Furukawa, H.; Yaghi, O. M. *J. Am. Chem. Soc.* **2009**, *131*, 9492−9493.

(31) Hong, D.-Y.; Hwang, Y. K.; Serre, C.; Férey, G.; Chang, J.-S. *Adv. Funct. Mater.* **2009**, *19*, 1537−1552.

(32) Shultz, A. M.; Sarjeant, A. A.; Farha, O. K.; Hupp, J. T.; Nguyen, S. T. *J. Am. Chem. Soc.* **2011**, *133*, 13252−13255.

(33) Tanabe, K. K.; Cohen, S. M. *Chem. Soc. Rev.* **2011**, *40*, 498−519.

(34) Fateeva, A.; Chater, P. A.; Ireland, C. P.; Tahir, A. A.; Khimyak, Y. Z.; Wiper, P. V.; Darwent, J. R.; Rosseinsky, M. J. *Angew. Chem., Int. Ed.* **2012**, *51*, 7440−7444.

(35) Foo, M. L.; Matsuda, R.; Kitagawa, S. *Chem. Mater.* **2014**, *26*, 310−322.

(36) Han, Y.; Li, J.-R.; Xie, Y.; Guo, G. *Chem. Soc. Rev.* **2014**, *43*, 5952−5981.

(37) Deria, P.; Mondloch, J. E.; Karagiaridi, O.; Bury, W.; Hupp, J. T.; Farha, O. K. *Chem. Soc. Rev.* **2014**, *43*, 5896−5912.

(38) Evans, J. D.; Sumby, C. J.; Doonan, C. J. *Chem. Soc. Rev.* **2014**, *43*, 5933−5951.

(39) Kitaura, R.; Onoyama, G.; Sakamoto, H.; Matsuda, R.; Noro, S.; Kitagawa, S. *Angew. Chem., Int. Ed.* **2004**, *43*, 2684−2687.

(40) Chandler, B. D.; Cramb, D. T.; Shimizu, G. K. H. *J. Am. Chem. Soc.* **2006**, *128*, 10403−10412.

(41) Wang, C.; Liu, D.; Lin, W. *J. Am. Chem. Soc.* **2013**, *135*, 13222−13234.

(42) Kalyanasundaram, K. *Photochemistry of Polypyridine and Porphyrin Complexes*; Academic Press: London, 1992.

(43) Juris, A.; Balzani, V.; Barigelletti, F.; Campagna, S.; Belser, P.; Zelewsky, A. V. *Coord. Chem. Rev.* **1988**, *84*, 85−277.

(44) Nazeeruddin, Md. K.; Kalyanasundaram, K. *Inorg. Chem.* **1989**, *28*, 4251.

(45) Hayami, S.; Murata, K.; Urakami, D.; Kojima, Y.; Akita, M.; Inoue, K. *Chem. Commun.* **2008**, 6510.

(46) Hayami, S.; Urakami, D.; Kojima, Y.; Yoshizaki, H.; Yamamoto, Y.; Kato, K.; Fuyuhiro, A.; Kawata, S.; Inoue, K. *Inorg. Chem.* **2010**, *49*, 1428.

(47) Krishnan, C. V.; Sutin, N. *J. Am. Chem. Soc.* **1981**, *103*, 2141−2142.

(48) Ziessel, R.; Hawecker, J.; Lehn, J.-M. *Helv. Chim. Acta* **1986**, *69*, 1065−1084.

(49) Goldsmith, J. I.; Hudson, W. R.; Lowry, M. S.; Anderson, T. H.; Bernhard, S. *J. Am. Chem. Soc.* **2005**, *127*, 7502−7510.

(50) Jasimuddin, S.; Yamada, T.; Fukujum, K.; Otsuki, J.; Sakai, K. *Chem. Commun.* **2010**, *46*, 8466−8468.

(51) Masaoka, S.; Sakai, K. *Chem. Lett.* **2009**, *38*, 182.

(52) Concepcion, J. J.; Jurss, J. W.; Norris, M. R.; Chen, Z.; Templeton, J. L.; Meyer, T. J. *Acc. Chem. Res.* **2009**, *42*, 1954.

(53) Duan, L.; Bozoglian, F.; Mandal, S.; Stewart, B.; Privalov, T.; Llobet, A.; Sun, L. *Nat. Chem.* **2012**, *4*, 418−423.

(54) Kent, C. A.; Mehl, B. P.; Ma, L.; Papanikolas, J. M.; Meyer, T. J.; Lin, W. *J. Am. Chem. Soc.* **2010**, *132*, 12767−12769.

(55) Kent, C. A.; Liu, D.; Ma, L.; Papanikolas, J. M.; Meyer, T. J.; Lin, W. *J. Am. Chem. Soc.* **2011**, *133*, 12940−12943.

(56) Kent, C. A.; Liu, D.; Meyer, T. J.; Lin, W. *J. Am. Chem. Soc.* **2012**, *134*, 3991−3994.

(57) Wang, J.-L.; Wang, C.; Lin, W. *ACS Catal.* **2012**, *2*, 2630−2640.

DOI: 10.1021/ic5021302
*Inorg. Chem.* 2015, 54, 2522−2535

(58) Beves, J. E.; Constable, E. C.; Housecroft, C. E.; Kepert, C. J.; Price, D. J. *CrystEngComm* **2007**, *9*, 456−459.

(59) Han, F. S.; Higuchi, M.; Ikeda, T.; Negishi, Y.; Tsukuda, T.; Kurth, D. G. *J. Mater. Chem.* **2008**, *18*, 4555−4560.

(60) Zhang, S.; Han, L.; Li, L.; Cheng, J.; Yuan, D.; Luo, J. *Cryst. Growth Des.* **2013**, *13*, 5466−5472.

(61) Kobayashi, A.; Sugiyama, A.; Ohba, T.; Suzuki, Y.; Chang, H.-C.; Kato, M. *Chem. Lett.* **2014**, *43*, 1070−1072.

(62) Kobayashi, A.; Suzuki, Y.; Ohba, T.; Noro, S.; Chang, H.-C.; Kato, M. *Inorg. Chem.* **2011**, *50*, 2061−2063.

(63) Kobayashi, A.; Ohba, T.; Saitoh, E.; Suzuki, Y.; Noro, S.; Chang, H.-C.; Kato, M. *Inorg. Chem.* **2014**, *53*, 2910−2921.

(64) Gustafsson, M.; Bartoszewicz, A.; Martín-Matute, B.; Sun, J.; Grins, J.; Zhao, T.; Li, Z.; Zhu, G.; Zou, X. *Chem. Mater.* **2010**, *22*, 3316−3322.

(65) Lee, W. R.; Ryu, D. W.; Lee, J. W.; Yoon, J. H.; Koh, E. K.; Hong, C. S. *Inorg. Chem.* **2010**, *49*, 4723−4725.

(66) Duan, J.; Higuchi, M.; Foo, M. L.; Horike, S.; Rao, K. P.; Kitagawa, S. *Inorg. Chem.* **2013**, *52*, 8244−8249.

(67) Fukushima, T.; Horike, S.; Inubushi, Y.; Nakagawa, K.; Kubota, Y.; Takata, M.; Kitagawa, S. *Angew. Chem., Int. Ed.* **2010**, *49*, 4820−4824.

(68) Burrows, A. D. *CrystEngComm* **2011**, *13*, 3623−3642.

(69) Wang, C.; Xie, Z.; deKrafft, K. E.; Lin, W. *J. Am. Chem. Soc.* **2011**, *133*, 13445−13454.

(70) Fang, Z.; Dürholt, J. P.; Kauer, M.; Zhang, W.; Lochenie, C.; Jee, B.; Albada, B.; Metzler-Nolte, N.; Pöppl, A.; Weber, B.; Muhler, M.; Wang, Y.; Schmid, R.; Fischer, R. A. *J. Am. Chem. Soc.* **2014**, *136*, 9627−9636.

(71) Wang, C.; Liu, D.; Xie, Z.; Lin, W. *Inorg. Chem.* **2014**, *53*, 1331−1338.

(72) Matthews, C. J.; Elsegood, M. R. J.; Bernardinelli, G.; Clegg, W.; Williams, A. F. *Dalton Trans.* **2002**, 492−497.

(73) Eskelinen, E.; Luukkanen, S.; Haukka, M.; Ahlgrén, M.; Pakkanen, T. A. *J. Chem. Soc., Dalton Trans.* **2000**, 2745−2752.

(74) Christopoulous, K.; Karidi, K.; Tsipis, A.; Garoufis, A. *Inorg. Chem. Commun.* **2008**, *11*, 1341−1346.

(75) *CrystalClear*; Molecular Structure Corp.: Orem, UT, 2001.

(76) SIR2004: Burla, M. C.; Caliandro, R.; Camalli, M.; Carrozzini, B.; Cascarano, G. L.; De Caro, L.; Giacovazzo, C.; Polidori, G.; Spagana, R. *J. Appl. Crystallogr.* **2005**, *38*, 381.

(77) SHLEX97: Sheldrick, G. M. *Acta Crystallogr., Sect. A* **2008**, *64*, 112.

(78) *CrystalStructure 4.0*, Crystal Structure Analysis Package; Rigaku Corp.: Tokyo, 2000.

(79) PLATON: Spek, A. L. *J. Appl. Crystallogr.* **2003**, *36*, 7−13.

(80) Smith, D. K. *J. Chem. Educ.* **1977**, *54*, 540−542.

(81) Shannon, R. D. *Acta Crystallogr.* **1976**, *A32*, 751−767.

DOI: 10.1021/ic5021302
*Inorg. Chem.* 2015, 54, 2522−2535